ADVANCED PHYSICS RESEARCH Open Access
www.advphysicsres.com

Hysteresis, Rectification, and Relaxation Times of Nanofluidic Pores for Neuromorphic Circuit Applications

Juan Bisquert

Based on the emergence of iontronic fluidic components for brain-inspired computation, the general dynamical behavior of nanopore channels is discussed. The main memory effects of fluidic nanopores are obtained by the combination of rectification and hysteresis. Rectification is imparted by an intrinsic charge asymmetry that affects the ionic current across the nanopores. It is accurately described by a background conductivity and a higher conduction branch that is activated by a state variable. Hysteresis produces self-crossing diagrams, in which the high current side shows inductive hysteresis, and the low current side presents capacitive hysteresis. These properties are well captured by measurements of impedance spectroscopy that show the correspondent spectra in each voltage wing. The detailed properties of hysteresis and transient response are determined by the relaxation time of the gating variable, that is inspired in the Hodgkin-Huxley neuron model. The classification of effects based on simple models provides a general guidance of the prospective application of artificial nanopore channels in neuromorphic computation according to the measurement of complementary techniques.

1. Introduction

The proliferation of artificial intelligence (AI) and automation gives rise to increased demand for electricity. Neuromorphic computing systems offer substantial promise in surpassing the constraints linked with conventional AI algorithms.[1–4] Neuromorphic devices strive to emulate key aspects of the brain's structure and dynamics in order to reproduce its distinctive functional capabilities, including robust learning and computational power. Physical neural networks combine memory and processing reducing significantly the energy cost of computation, which is a central criterion for the future development of massive AI systems.[5] Many approaches to brain-inspired computation systems are based on solid state memristive systems[6,7] and electrochemical transistors.[5,8]

Alternatively, biomimetic material devices provide the ability to replicate diverse neuromorphic functions, encompassing artificial synapses, neurons, combined into computational networks. Ionic current rectification represents a frequently observed occurrence in both naturally occurring protein ion channels and synthetic nanopores.[9] Extensive investigation has been conducted on these systems owing to their crucial involvement in various physiological processes within living organisms, such as elucidated in the Hodgkin and Huxley (HH) model detailing the dynamics of biological neurons.[10–14] Fluidic and artificial solid-state nanopores and nanochannels can function as synthetic analogs to protein ion channels and have been customized for integration into computational networks.[15–33]

Rectification, transient current responses, and hysteresis are central properties for biomimetic iontronic elements. The diode-like response of nanopores has been researched widely, using channel morphologies that produce asymmetrical electrical transport.[34–44] When the scan frequency is increased, the current changes according to the direction and velocity of the dynamic voltage sweep scheme. This is the property of hysteresis.[45] The use of a given device as a synapse relies on dynamic memory facilitated by rectification and hysteresis.[19] The application of nanopores as spiking neurons requires in addition negative resistance features.[17,46]

In this paper, we summarize the application of nanopore channels in neuromorphic circuits. We explain simple models that describe the dynamical rectification, hysteresis, and transient current properties of fluidic nanopores, based on general approaches to HH model and memristor modeling. Impedance spectroscopy is a power tool to connect synaptical and neuron dynamics to the device mechanisms.[47–49] We illustrate different kinetic regimes that are well described by characteristic impedance spectra as determined by voltage-dependent relaxation times. We provide a reference structure of dynamical equations that can be adapted to

J. Bisquert
Institute of Advanced Materials (INAM)
Universitat Jaume I
Castelló 12006, Spain
E-mail: bisquert@uji.es
J. Bisquert
Instituto de Tecnología Química (Universitat Politècnica de València-Consejo Superior de Investigaciones Científicas)
Av. dels Tarongers, València 46022, Spain

The ORCID identification number(s) for the author(s) of this article can be found under https://doi.org/10.1002/apxr.202400029

DOI: 10.1002/apxr.202400029

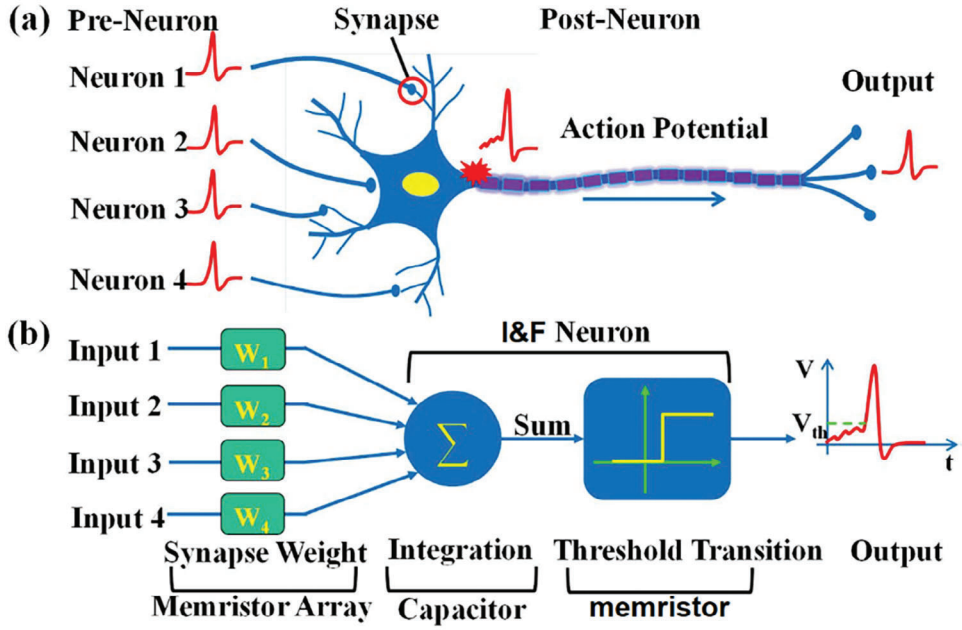

Figure 1. a) A biological neuron receives inputs from other neurons by interconnected synapses. b) A representative threshold-switching memristor neuron for accumulating inputs generated by different pre-neurons. Reproduced with permission.[88] Copyright 2028, IEEE.

specific situations. The interpretation of complementary types of measurements produces an understanding of the factors controlling resistive switching and memristive volatility that are the essential features for the integration of the elementary channels in larger units of liquid-based operational computational networks.

2. Neuromorphic Circuits

Neuromorphic engineering aims to create artificial neural systems, such as computational arrays of synapse-connected artificial neurons, and retinomorphic vision systems.[50–52] The future trajectory of artificial neural networks, drawing inspiration from the human brain, entails a substantial enhancement in comprehending the operations of the nervous system, encompassing its communication mechanisms and functionalities. Up to date, the majority of neuromorphic circuits are built with CMOS technologies.[53] However, the natural brain functionalities are made of protein ionic channels and chemical signaling. Several organic-based materials with high biological fidelity are explored for computational networks.[4,54–56] Ionic nanopores provide the opportunity for the biology-inspired neuromorphic systems based on fully liquid circuits.

The neuron serves as the fundamental unit for encoding, transmitting, and decoding information within the brain.[11] Neurons communicate via spiking signals, distinguished by their sparse, pulsed, and frequency-modulated attributes. These spikes originate from voltage-gated ion channels within the neuron membrane. The basic structure of neural networks, composed by neurons and synapses is indicated in **Figure 1**. Through the coordinated action of ion channels, neurons generate sequences of single-bit impulses known as action potentials, which are then transmitted to adjacent neurons via synapses.[11,13] A neuron integrates the incoming signals and fires in turn if a threshold is achieved.

2.1. Synapses

One of the most challenging aspects of emulating brain-like computation lies in replicating biological synapses, which depend on ions and the release of neurotransmitters to control response delays.[57] The synapsis functions are essential for learning, memory, and inference in the human brain, aiding real-time information processing and transmission. Neuronal connections can strengthen or weaken under high- or low-frequency stimulation, respectively, as they are highly sensitive to activity-induced patterns (synaptic plasticity). These properties are outlined in **Figure 2** for halide perovskite artificial synapses.[58] The brain's ability to memorize and learn by spike-timing dependent plasticity (STPD) is produced by neuroplasticity functions of synapses, known as long-term potentiation and depression. These properties provide the basis for the development of artificial neurons and synapses.[55,56]

2.2. Memristors

Memristors are highly nonlinear systems that show a change of the electrical resistance under voltage cycling.[59–61] Memristors can be switched between two states of conductance, with high and low resistance.[62,63] Dynamical models of memristors serve as inspiration for the description of nanoporous fluidic channels.[64–68] The operation of a memristor as synapse in a neural network, requires specific memory and volatility

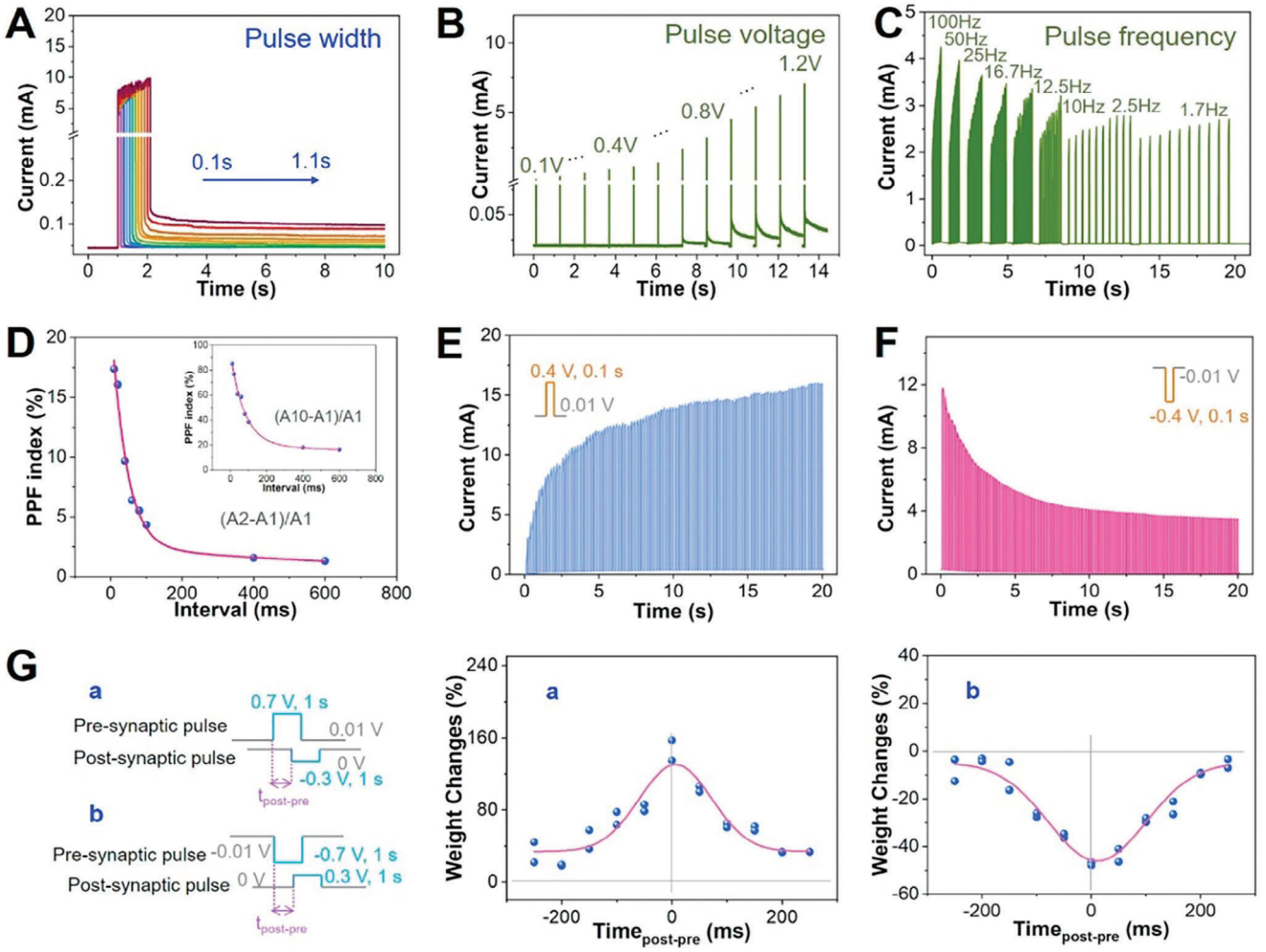

Figure 2. Synaptic Plasticity of Perovskite-based Artificial Synapses. A) Excitatory postsynaptic current (EPSC) according to the pulse duration from 0.1 to 1.1 s (spike amplitude: 0.65 V). B) EPSC according to the pulse voltage amplitude from 0.1 to 1.2 V (spike duration 0.5 ms). C) EPSC according to the pulse frequency from 1.7 to 100 Hz. D) Pulse paired facilitation (PPF) index versus time interval between two successive pulses (−0.45 V, 0.05 s duration). Inset: PPF index versus time interval between the 1st and the 10th pulse (−0.45 V, 0.05 s duration). E) Emulated EPSC plasticity using positive pulses (0.4 V; pulse width, 0.1 s; pulse interval, 0.1 s). F) Emulated EPSC plasticity using negative pulses (−0.4 V; pulse width, 0.1 s; pulse interval, 0.1 s). G) Implementation of STDP-like behaviors in the perovskite-based artificial synapses: the symmetric Hebbian rule (a), and the symmetric anti-Hebbian rule (b). The blue dots demonstrate the experimental data and the pink lines are fitting to dots. The left diagram reveals pre-synaptic and post-synaptic spikes. Synaptic plasticity of perovskite-based artificial synapses. Reproduced with permission.[58] Copyright 2020, Elsevier.

properties to establish the required STDP according to the network operation.[59,69–72]

2.3. Networks

Spiking neural networks (SNN) operate by discrete spikes (repetitive action potentials), as shown in **Figure 3**a.[73] Many practical realizations of the computation networks rely on memristors in crossbar arrangement as shown in Figure 3b.[74] The input is given by the voltage in each line, and the "vector-matrix" multiplication is completed by the current collected from each line completes by application of circuit laws. The operation of a 2 × 2 network for pattern recognition is presented in **Figure 4**,[75] showing how the memristors combine the incoming spiking signals to produce the required output.

3. Neuron Models

3.1. Hodgkin and Huxley Model

To emulate the physical behaviors of neurons and synaptic devices, researchers leverage insights from natural systems. In the 1950s, Hodgkin and Huxley (HH) developed a model based on a set of differential equations, laying the foundation for understanding neuronal behavior.[10,12–14] The electrical structure of the HH model is shown in **Figure 5**. The HH model's significant success lies in its precise depiction of the coordinated operation of ion channels, accurately capturing the temporal dynamics of action potentials. This model has been extended incorporating different elements of complexity for simulations of neural systems,[13,76–80] to reach high level of fidelity to the spiking patterns in biological processes.[81–83]

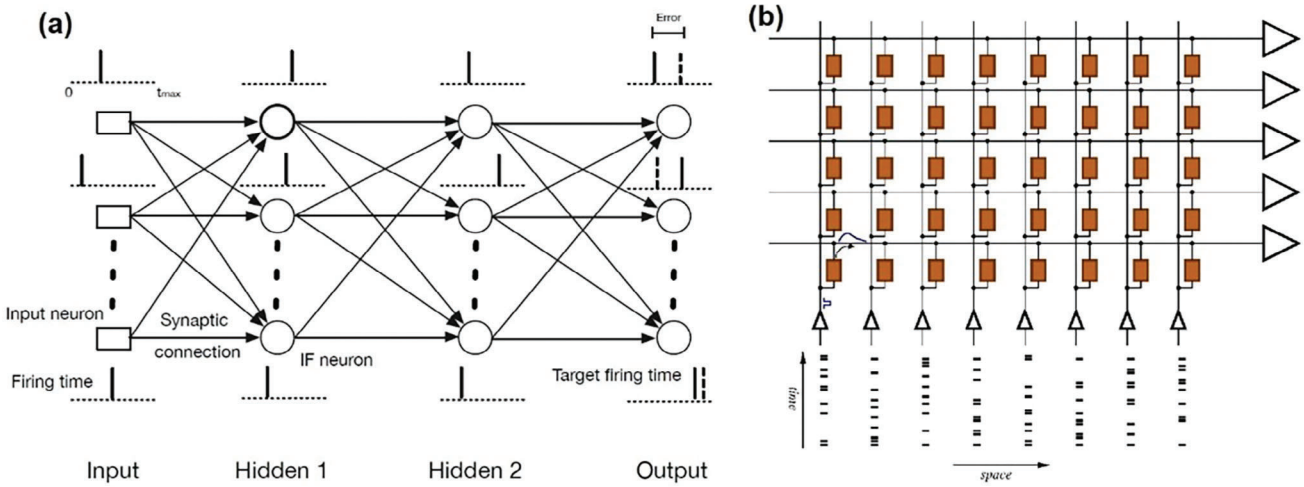

Figure 3. a) SNN with two hidden layers. The input layer converts the input data into a spike train (using the temporal time-to-first-spike coding) and sends it to the next layer. Spikes are propagated through the network and reach the output layer. The output layer computes the errors with respect to the target firing times, and then, synaptic weights are updated using the temporal error backpropagation. (Figure 1 in[73]) b) SNN crossbar with synaptic memristors. At the bottom is the input line from spiking neurons, that is converted in output signals (right column) toward the next neuronal layer, according to the dynamic summation of the memristors in each row.

The HH model contains a combination of rectifying ion channels with time-delayed properties that are an essential reference for the nanopore channel model approaches that we will discuss later. Although there are excellent textbooks and accounts on the time domain response properties of the HH model,[11,13,14,84] here we survey the model components in some detail.

The structure of the model is as follows

$$I_{tot} = C_m \frac{du}{dt} + g_{Na} m^3 h \left(u - E_{Na}\right) + g_K n^4 \left(u - E_K\right) + g_{leak} \left(u - E_{leak}\right) \tag{1}$$

$$\tau_m (u) \frac{dm}{dt} = m_{eq} (u) - m \tag{2}$$

$$\tau_h (u) \frac{dh}{dt} = h_{eq} (u) - h \tag{3}$$

$$\tau_n (u) \frac{dn}{dt} = n_{eq} (u) - n \tag{4}$$

Equation (1) relates the current I_{tot} and the voltage V across the neuron wall. We use the voltage u

$$u = V - V_R \tag{5}$$

where $V_R = -65$ mV is the rest voltage of the membrane.

Equation (1) contains a capacitive charging with the capacitance C_m of the neuron wall. The next three terms correspond to generalized Ohm's law where $(u - E_i)$ is the driving force. Each type of channel is selective to conduct one type of ion, with conductance g_{Na}, g_K, g_{leak} where the latter is a leak term, and the E_{Na}, E_K, E_{leak} are the equilibrium potentials at which each of the currents is balanced by ionic concentration differences across the membrane. The current across the channel is also controlled by gating variables m, h, n, that vary between 0 and 1 and represent sodium channel conductance activation, sodium channel deactivation, and K channel activation respectively. The temporal evolution of these gating variables is determined by the kinetic relaxation Equations (2–4). The kinetic times τ_m, τ_h, τ_n are a function of the voltage u, and so are the equilibrium functions m_{eq}, h_{eq}, n_{eq} of the activation variables.

The relaxation equations of HH model in Equations (2–4) can be written[84]

$$\frac{dm}{dt} = \alpha_m (1 - m) - \beta_m m \tag{6}$$

$$\frac{dh}{dt} = \alpha_h (1 - h) - \beta_h h \tag{7}$$

$$\frac{dn}{dt} = \alpha_n (1 - n) - \beta_n n \tag{8}$$

The transfer rate coefficients α_i and β_i that are voltage dependent and time independent, as follows:[11,47]

$$\alpha_m = \frac{0.1 (25 - u)}{e^{\frac{25-u}{10}} - 1} \tag{9}$$

$$\beta_m = \frac{4}{e^{\frac{u}{18}}} \tag{10}$$

$$\alpha_h = \frac{0.07}{e^{\frac{u}{20}}} \tag{11}$$

$$\beta_h = \frac{1}{e^{\frac{30-u}{10}} + 1} \tag{12}$$

$$\alpha_n = \frac{0.01 (10 - u)}{e^{\frac{10-u}{10}} - 1} \tag{13}$$

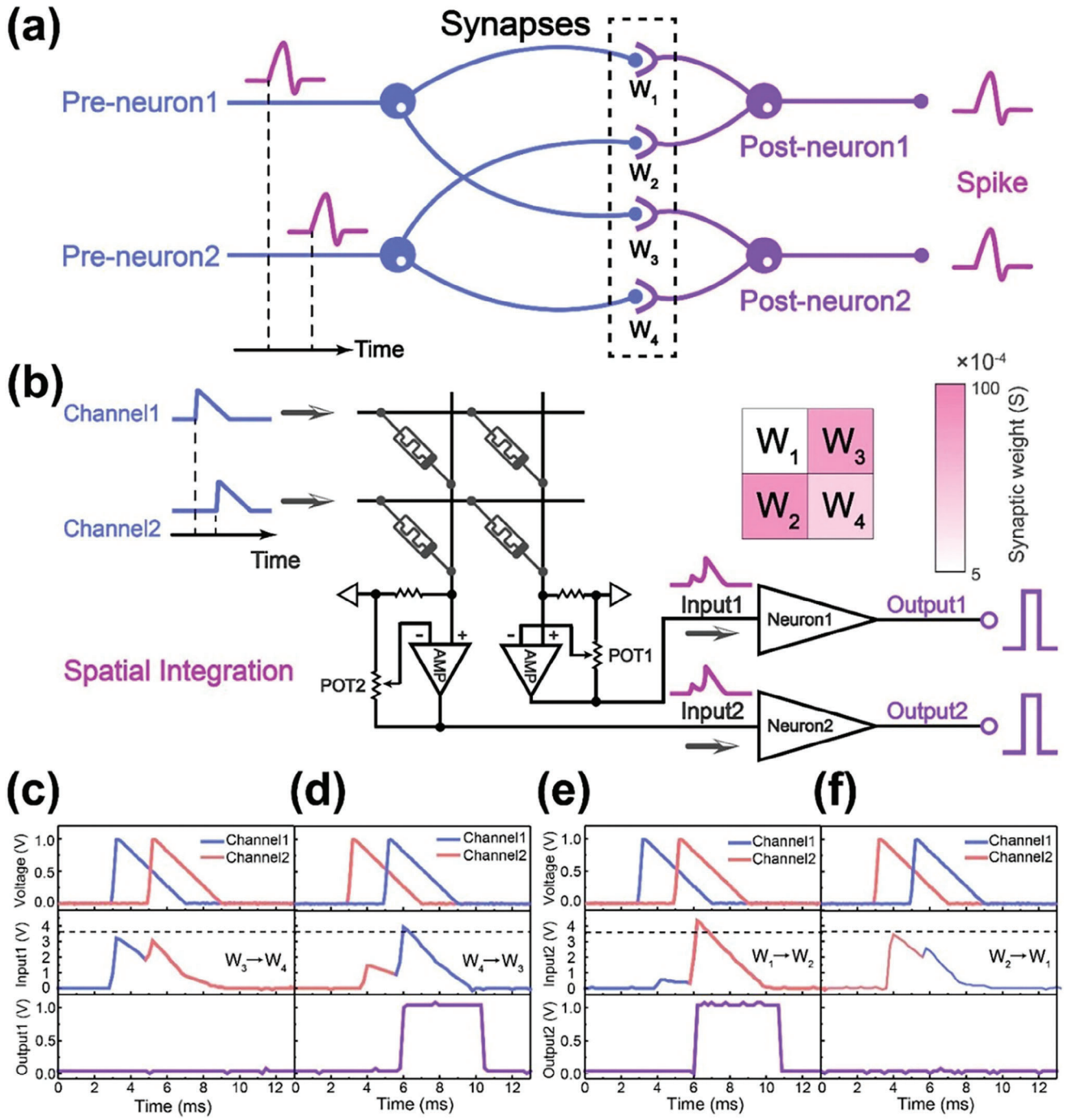

Figure 4. a) Conceptual scheme of a spatiotemporal network which is composed of 2 Pre-neurons and 2 Postneurons. The Pre- and Post-neurons connect to each other through 4 synapses, framing a simple spiking neural network (SNN). b) Schematic diagram of the circuit realization of the spatiotemporal network in (a), and synaptic weights maps of the synaptic array. Neuron1 and Neuron2 are the simplified schematic diagrams of the LIF model. The stimulus signals (voltage signals come from Channel1 and Channel2) are integrated on the synaptic array. Then the currents flowing through the synaptic array are amplified by the amplifiers and converted into voltages to stimulate the neurons. c) Output of Neuron1 in an input sequence of Channel1 – Channel2. d) Output of Neuron1 in an input sequence of Channel2 – Channel1. e) Output of Neuron2 in an input sequence of Channel1 – Channel2. f) Output of Neuron2 in an input sequence of Channel2 – Channel1. Reproduced with permission.[75] Copyright 2020, Elsevier.

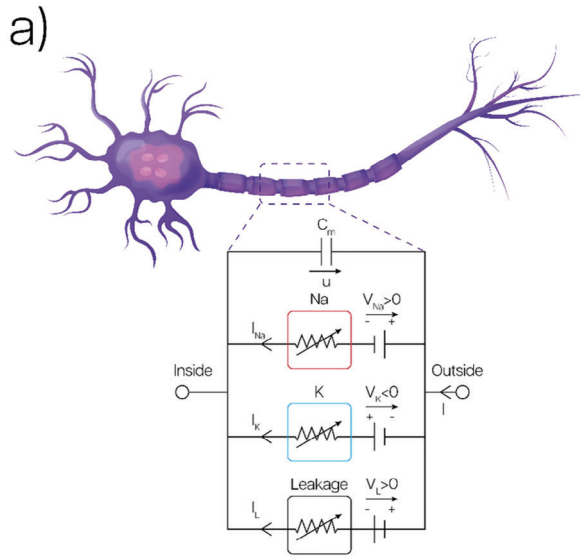

Figure 5. a) Electrical structure of HH model consists on the membrane capacitance, two voltage-gated ionic (sodium and potassium) channels with opposite polarities, and a leak channel of constant conductivity. Reproduced with permission.[17] Copyright 2023, American Chemical Society.

$$\beta_n = \frac{0.125}{e^{\frac{u}{80}}} \tag{14}$$

The equilibrium values of the gating variables $\gamma_i = m, h, n$ have the values

$$\gamma_i = \frac{\alpha_i}{\alpha_i + \beta_i} \tag{15}$$

These functions are shown in **Figure 6**a.

Based on the equilibrium values we can form the voltage dependence of the stationary current, from Equation (1), and it is shown in Figure 6b. Note the clear rectification form of the current that intercepts the horizontal axis when the membrane voltage V is at the resting potential V_R. Accordingly, the conductance

$$g_{dc} = \frac{dI_{tot}}{du} \tag{16}$$

makes a transition from a low value to a large value, as shown in Figure 6c.

It is interesting to consider the current across each type of channel, as shown in Figure 6d. Each current crosses the axis at the respective equilibrium potential according to Equation (1). The potassium current (orange line) shows a large increase above E_K, although a small spike is observed in Figure 6e. The sodium current (blue line) shows the same spike, though larger, but the rising positive current is suppressed by the deactivation variable h. The dashed blue line is the current that would happen without the deactivation effect. We remark that the sodium current has the same polarity as the potassium current, but the hypothetical (unblocked) sodium current is larger due to higher conductance of the sodium channel. These features will be further explained in Section 6.

The relaxation times in (2–4) take the form

$$\tau_i = \frac{1}{\alpha_i + \beta_i} \tag{17}$$

They are represented in Figure 6f,g.

While HH model represents the original model system of the squid axon, research in recent decades has produced a large class of neuron models to represent the observations.[13] For a better understanding of the features of the relaxation times in advanced neuron simulation we show in **Figure 7** the Reduced Tong Model (RTM)[82] that uses activation and inactivation variables for nine ion channels, and the Full Tong Model (FTM)[81,83] that comprises a total of thirteen ion channels selective to Ca_2^+, Na^+, Cl^- and K^+. **Figure 8** shows the current and relaxation times of activation processes of the fast K^+ current.[85]

3.2. Emulating Neurons

There are different ways to make neurons for brain-like computation with SNN. The specific choice of neuron model type relies on the requirements of data and type of computation.[86,87] The main types of neurons are the following:

The *event-based neurons* are the simplest class of neurons, amply used in most computational methods. The integrate-and-fire (IF) model, and the modified leaky integrate and fire (LIF) model,[75,88] provide a realization of spiking. The accumulation of charge represents the integration function of the neuron, that fires when a voltage threshold is reached.[86,89]

Bio-physical models are based on the standard HH formulation[14] and its expansion to broader classes of neurons with varied types of firing patterns.[13,76,77] In these models, the electrical response is smooth as obtained by a set of nonlinear differential equations, which capture the progression of action potentials over time in biological cells. In this approach one can find direct reproduction of the two-channel HH model using different material platform devices, that achieve high biological fidelity.[90–93] HH model contains a Hopf bifurcation causing limit cycle sustained oscillations.[94] There is a minimum fire frequency ω_0 at the bifurcation, and below this value there is no firing at all. So, there is either rest or spiking at some minimum frequency or higher.

Based on the structure of bifurcation, one can construct simpler systems than HH based on a single channel, that produce effective spiking at $\omega > \omega_0$.[46,67,95,96] A range of elements is needed for obtaining such structure in the model, including a capacitance, a chemical inductor, and a negative resistance.[46]

4. Rectification in Nanopores Channels

Rectification of ionic current in nanopores is a property that has been amply investigated.[34–40] It consists on obtaining a much larger current in one voltage direction (forward) than in the other one (reverse). Rectification is represented characteristically in **Figure 9**a in which the slow curve measured at the frequency $f_\Omega = 0.01$ Hz shows large conductance at positive bias and low conductance at negative voltage. The primary cause of

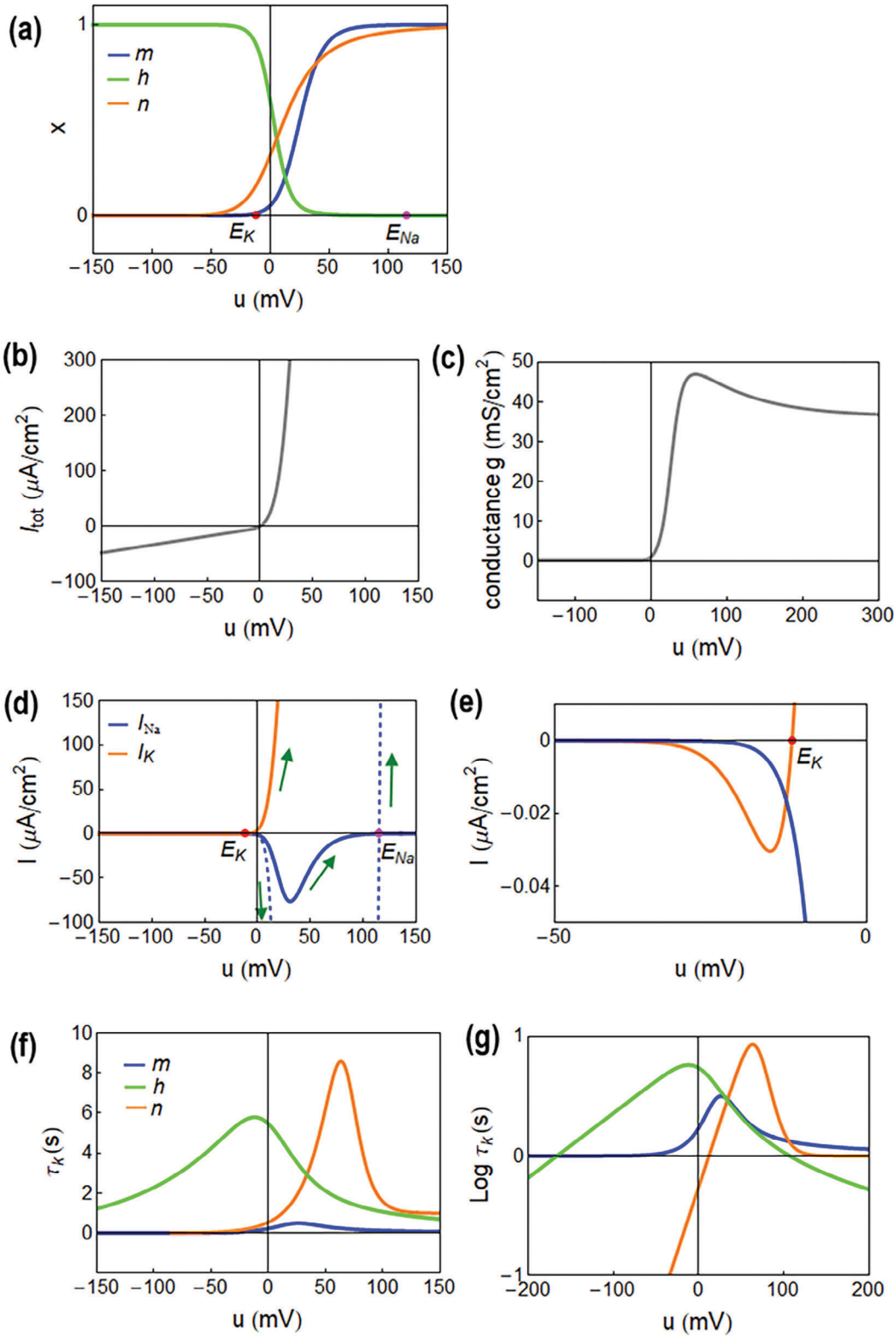

Figure 6. a) Equilibrium values of the HH gating variables dependence on membrane potential $u = V - V_R$. The resting potentials are $E_{Na} = V_R + 115$ mV, $E_K = V_R - 12$ mV are indicated by dots. b) Total equilibrium current. The conductances are $g_{Na} = 120$, $g_K = 36$ mS cm^{-2}, $g_{leak} = 0.3$ mS cm^{-2} and $E_L = V_R + 10.6$ mV. c) Total conductance. d) Equilibrium current of the sodium and potassium channels. The dashed line is the sodium current without the effect of the deactivation variable ($h = 1$). The arrows indicate the direction of increasing voltage. The negative resistance feature of the potassium current is shown on smaller scale in (e). f) Relaxation times in linear scale and g) in logarithmic scale in a wider potential range.

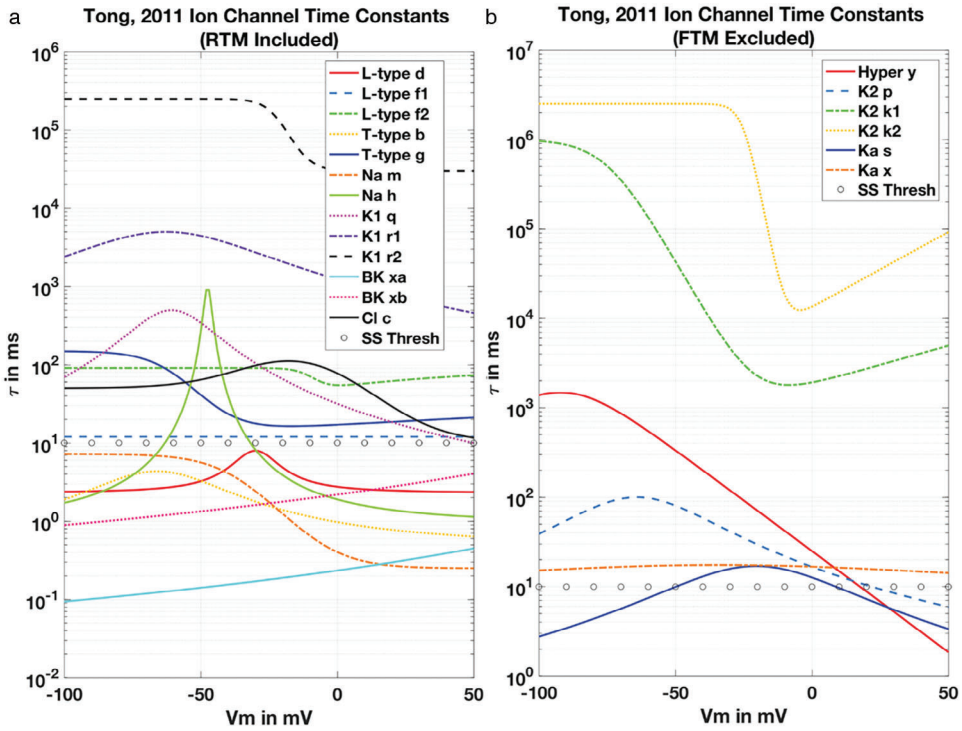

Figure 7. a) Suite of τ values as given for the Reduced Tong Model (RTM) family of ion channels and the corresponding activation and inactivation variables. Note extraordinary range on logarithmic scale over six orders of magnitude from 10−1 milliseconds for the BK-channel xb variable (teal trace) to as high as 100 s for the K+ channel variable r1 (dashed black trace). Each variation over membrane potential V_m are computed from the functional dependencies as given in the Full Tong Model (FTM), and selected channels in the RTM version appear here as described in text. The rough threshold for consideration of steady-state approximation partitioning the suite of these variables is at 10 ms (open circles), that is also sensitive to the range of V_m encountered during simulation. b) Corresponding suite of τ values for the FTM but excluded mechanisms from the final RTM. Note extraordinary range of time scales but shifted up around two orders of magnitude compared with the RTM suite. Reproduced with permission,[82] licensed under a Creative Commons Attribution (CC BY 4.0) license.

rectification in artificial pores stems from the uneven geometry of the nanopore and/or the configuration of surface charges, including their respective polarities, along the sidewalls of the nanopore.

We also observe in Figure 9a an opening of the current-voltage curve at higher frequencies, with associated decrease of the effective conductance, and a dependence of the amplitude of the voltage scan in Figure 9b. These properties are of kinetic origin, they are generally termed hysteresis and will be discussed in Section 7.

There are many different systems and technologies to fabricate rectifying nanopores.[9,34,40,43,97,98] In one type of fabrication process, the bombardment of ions through the polymer film leads to the formation of latent ion tracks. These are converted into asymmetric pores of conical shape by the track-etching procedure.[99,100] The current-voltage curves of a nanoporous membrane obtained by irradiation of polyimide foils are shown in Figure 9. The track-etching causes the formation of carboxylate groups that give negative charge densities on the pore surface.[101] The interaction between the mobile electrolyte ions and the pore fixed charges in the vicinity of the pore tip govern the current-voltage characteristics of the membrane.[30] When the membrane is placed in an electrochemical cell that separates two KCl solutions, charge carriers accumulate in the pore tip region at positive voltages, while the carrier concentration in this region is depleted at negative voltages.

Figure 10 shows the nanopores made from anodic oxides of alumina (Al_2O_3) generated from valve metals via anodization.[44,97,102–105] In this case the pore is blocked at the bottom but the ions diffuse across the barrier oxide layer. A selective flow of ions such as potassium (K^+) and chloride (Cl^-) ions from salt electrolytes across the bottom barrier of the nanopores results in the characteristic ionic current rectification.

Another significant technology is the glass nanopores as shown in **Figure 11**.[35,106–108] Figure 11a shows the dependence on hysteresis on scan rate, with increasing modulation of the conductivity. Furthermore the impedance measurements in Figure 11b,c show the appearance of an inductor feature that has important implications for the interpretation of hysteresis as discussed later in this paper. Note that the current in Figure 11a is much smaller than the previous examples as it corresponds to a single pore while the membranes in Figures 9 and 10 contain hundreds of pores.

5. Functional Description of Rectification

There are many mechanisms of current rectification, for example the electron barrier in a semiconductor diode.[109] Numerously

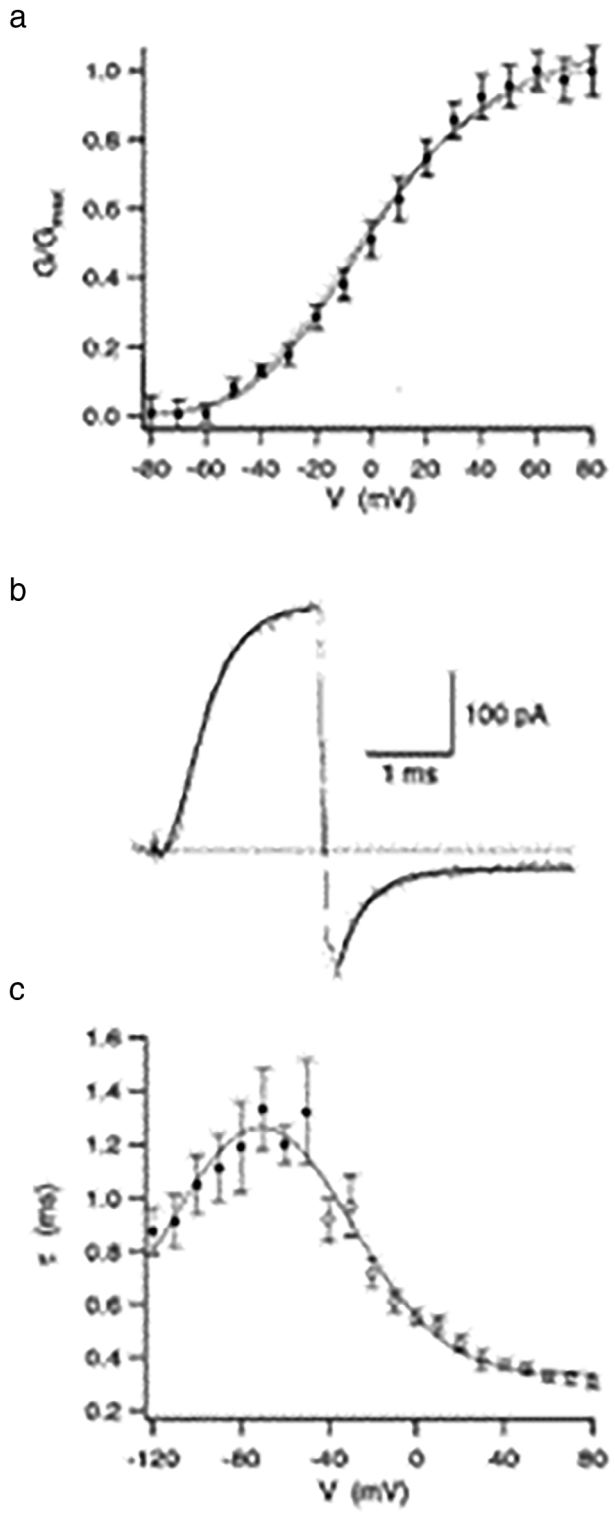

Figure 8. Activation kinetics of the fast K^+ current. a) Activation curve fit of the conductance to the Boltzmann equation. b) Current recording of the activation and deactivation processes of the fast K^+ current. The fast outward current was generated by a 2 ms voltage step to +80 mV following a 50 ms pre-pulse to -110 mV. The voltage was then stepped to -120 mV to record the deactivation kinetics. c) Activation (○) and deactivation (•) time constants determined from traces similar to the one displayed in (b). The smooth line is the curve fit to the equation: $C_1+C_2\exp(-[(V-C_3)/C_4]2)$, with $C_1 = 0.34 \pm 0.03$ ms, $C_2 = 0.92 \pm 0.04$ ms, $C_3 = -71 \pm 2$ mV and $C_4 = 59 \pm 4$ mV. Reproduced with permission,[85] licensed under a Creative Commons Attribution (CC BY 4.0) license.

reported experimental data on rectification of fluidic nanopores have been described in terms of advanced models that represent several physical features, such as geometry of the pores, charge distribution, electrolyte concentration, and the gradient along the pore.[41,110,111] Here we discuss a well-established general model for the functional dependence of a rectifying ion channel that provides the essential elements of the dynamical behavior.[112–117] It is based on the generalized Ohm's law formulated by HH model,[13] combined by a voltage-gated process typical of activation and inactivation in channel gates. This approach is also used in several solid state memristor models.[64,66,118–120]

Inspired in Equation (1), we propose a model for the stationary current I_{dc} as a function of voltage u in a single rectifying pore

$$I_{dc}(u) = \left[g_L + x_{eq}(u)\left(g_H - g_L\right)\right]\ \left(u - E_0\right) \tag{18}$$

The term $(u - E_0)$ in Equation (18) is the driving force for the current.[10,77] The term in square parenthesis is a conductance that makes a change from a low value g_L to a high value g_H. This happens when the activation function passes from $x_{eq} = 0$ to $x_{eq} = 1$. This is a central property of the neuron model as shown in Figure 6c. In our model the current in the activated state is

$$I_A(u) = g_H\ \left(u - E_0\right) \tag{19}$$

and the current in the deactivated state is

$$I_D(u) = g_L\ \left(u - E_0\right) \tag{20}$$

We adopt here the standard form of the activation variable

$$x_{eq} = \frac{1}{1 + e^{-\left(u - V_B\right)/V_m}} \tag{21}$$

where V_B is a threshold potential, and the voltage V_m describes the steepness of the transition. V_m can be identified with the thermal voltage in some contexts, then Equation (21) corresponds open channel probability[114,121] with a Boltzmann distribution that represents the fraction of active conducting channels.[37] As an example, x can be related to the fraction of free ions in an ion channel.[16] The logistic activation function (21) is amply used in memristor models.[64,66,68,118–120] In general the activation function has a sigmoidal form and depends on the particular systems, e.g. see Figure 6a.

The properties of the model are shown in **Figure 12**. Figure 12a shows the stationary current-voltage curve, Figure 12b shows the different components of the current, and Figure 12c shows the total conductance that is obtained by Equation (16).

The model is obeyed nearly ideally by nanopore channels of the type of Figure 9, as shown in **Figure 13**. The resistances measured either by impedance spectroscopy, or by the differential of the IV curve, show nearly constant wings at positive and low voltages.

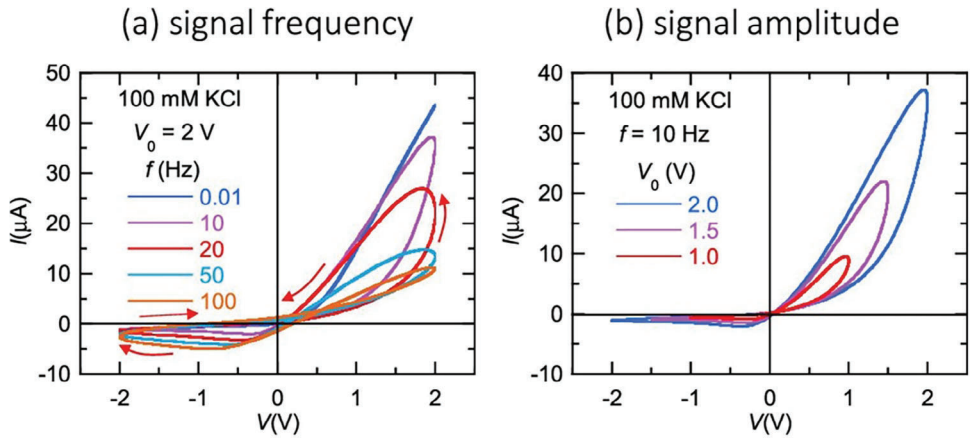

Figure 9. I–V curves for a multipore polyethylene terephthalate (PET) membranes membrane in 100 mM KCl solution at neutral pH, parametrically in the electrical potential scan rate, characterized by the signal frequency $f_\Omega = \Omega_s /2\pi$, obtained with a voltage amplitude 2 V. The arrows indicate the signal time evolution. I–V curves for different signal voltage amplitudes with c = 100 mM KCl solution at a signal frequency f = 10 Hz. a) Current response (left) to a sequence of 2 ms positive voltage pulses (right) showing a gradual conductance potentiation followed by a sequence of negative voltage pulses, which reset the multipore membrane to the low conductance state for neutral pH. b) Same experiment except for pH = 3.3. c) Same experiment except for pH = 2.0. In all cases, V0 = 1 V and c = 50 mM KCl. Reproduced with permission.[30] Copyright 2023, American Chemical Society.

6. The Negative Differential Resistance

The presence of a negative differential resistance in a system imparts an intrinsic instability that plays a central role in self-sustained oscillations.[46,122] This is a functional part of spiking neurons.[17,46,115,123] Therefore, we comment of the conditions in which the model of Equation (18) generates a negative resistance. The negative resistance features of HH model have been already remarked in Figure 6d,e.

As shown in **Figure 14**, when $V_B < E_0$ a negative resistance feature occurs by Equation (18). In contrast, in Figure 12 it is $V_B > E_0$ and no negative resistance happens. The negative resistance feature becomes large if the midpoint of the activation variable V_B is far below the intercept voltage E_0. The potassium channel in HH model contains a single activation variable, n. The negative resistance feature of Figure 6e corresponds to the interplay of characteristic voltages as in Figure 14. The negative current in Figure 6e is a very small feature because the equilibrium voltage E_K is very close to the midpoint of the gating variable n_{eq} in Figure 6a.

The sodium channel equilibrium voltage is, however, 100 mV above the midpoint of m_{eq} in Figure 6a. Therefore the current of the sodium channel present a large spike before the positive rising wing, as indicated in the dashed line of Figure 6d. However, the rise of the current is suppressed by the deactivation variable h, and the current dies off to zero. Physically this is an important part of the HH action potential, since the sodium channel first opens and then closes, and the potassium channel comes in later due to the delayed relaxation time in Figure 6f.

Figure 15 shows the negative resistance effect in polymer membrane nanopores as those of Figure 9.[37] The behavior observed in Figure 15 may not be explained by Figure 14 alone. It can be observed that the negative resistance in Figure 15 is obtained by suppression of the current of the activated state, after the normal rise starts, so that the current decreases to the inactivated state at some threshold voltage. This is the same structure of the current of the sodium channel in HH model, shown in Figure 6d.

To describe this behavior within the context of our model we extend Equation (18) as

$$I_{dc}(u) = \left[g_L + x_{eq}(u)\, y_{eq}(u)\left(g_H - g_L\right)\right]\ \left(u - E_0\right) \tag{22}$$

The deactivation function has the form

$$y_{eq} = \frac{1}{1 + e^{(u - V_C)/V_m}} \tag{23}$$

The generation of the negative resistance by the suppression of the raising current is shown in **Figure 16**. In the experimental results of Figure 15 the inactivation mechanism y_{eq} is caused by the presence of F^- ions in the low concentration (mM) range.[37]

7. General Characteristics of Hysteresis

As shown in Figure 9, hysteresis in current-voltage curves is well established in nanopore rectifiers.[19,107] We consider two voltage schemes to investigate hysteresis. In the electrochemical technique of cyclic voltammetry the voltage u is swept in the range $(-u_1, u_1)$ at a constant scan rate v_s as

$$u = v_s\, t \tag{24}$$

Alternatively, the voltage can be swept at a constant angular frequency Ω_s and frequency $f_\Omega = \Omega_s /2\pi$ as follows:

$$u = U_0\ \sin\left(\Omega_s t\right) \tag{25}$$

Comparing a full cycle in both systems, the following relationship holds between the velocity and the frequency:

$$\Omega_s = \frac{\pi v_s}{2u_1} \tag{26}$$

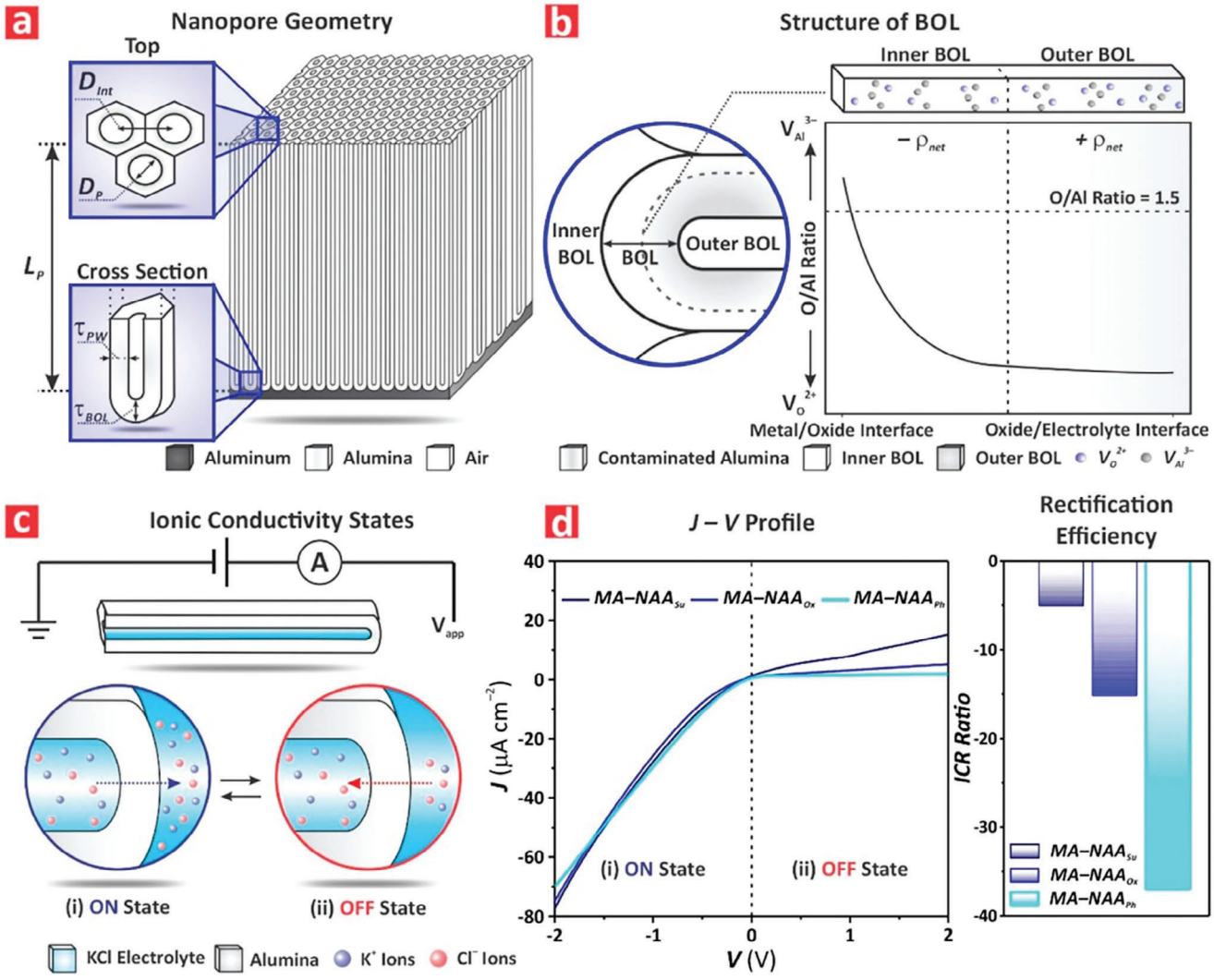

Figure 10. Iontronic characterization of nanoporous anodic alumina membranes produced at different anodization regimes during the selective etching process over time. a) Schematic depicting the structure of the membranes with a definition of their geometric features such as nanopore diameter (D_P), interpore distance (D_{Int}), nanopore length (L_P), pore wall thickness (τ_{PW}), and barrier oxide layer (BOL) thickness (τ_{BOL}). b) Schematic illustrating the evolution of the oxygen–aluminum vacancy ratio along the thickness of BOL. c) Schematics describing the flow of K^+ and Cl^- ions across the BOL under high and low conduction states. d) Representative J–V characteristics of the membranes produced by two-step mild anodization in sulfuric, oxalic, and phosphoric acid electrolytes (left) and their rectification ratio (right). Reproduced with permission.[44] Copyright 2023, American Chemical Society.

We discuss the hysteresis of ionic nanopores according to a general theory[45] that defines two types of hysteresis, capacitive hysteresis and inductive hysteresis. They are summarized in **Figure 17**. We consider them in turn.

7.1. Capacitive Hysteresis

The capacitance C is the charge Q to voltage V relation

$$Q = CV \tag{27}$$

The current under voltage sweep (24) is

$$I = \frac{dQ}{dt} = Cv_s \tag{28}$$

Thus, the capacitor introduces a hysteresis transient current in which the forward current is positive while the reverse current is negative. Hence the hysteresis loop around the stationary curve is clockwise, Figure 17b. As it is well known in electrochemistry, the capacitive current is simply proportional to the scan rate v_s.[124]

The small signal ac impedance of the capacitor at angular frequency ω is

$$Z = \frac{1}{i\omega C} \tag{29}$$

The basic capacitive circuit is shown in Figure 17c, and it explains the associated hysteresis behavior in Figure 17b.[45]

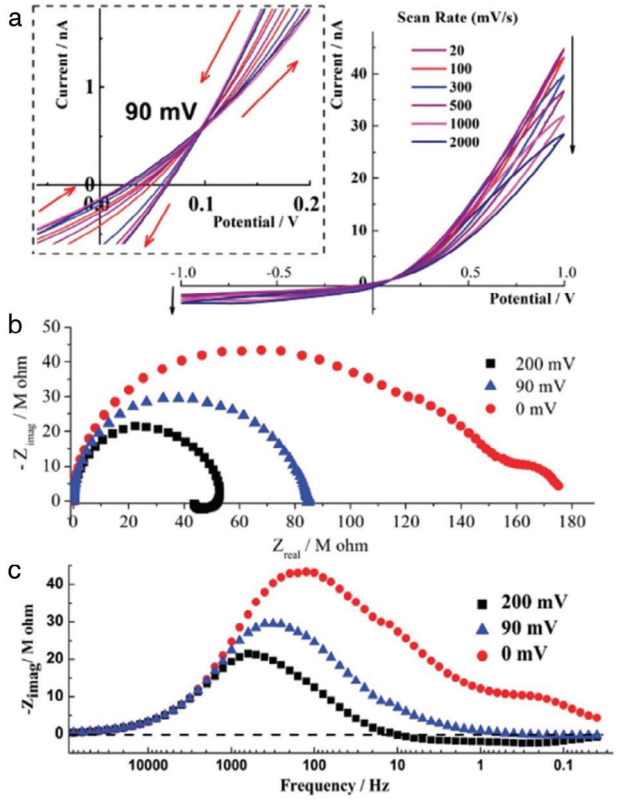

Figure 11. Dynamic characteristics of ion transport through conical glass nanopores. a) Overlaid I–V curves at different scan rates in 10 mM KCl. Cross-point potential remains at 90 mV at all scan rates. Black arrows next to the curves indicate changes in current with increase of scan rate. Red arrows in the inset illustrate direction of potential scan. Impedance spectra taken above, below, and at the cross-point potential are plotted in the form of Nyquist b) and Bode c) plots. Reproduced with permission.[35] Copyright 2012, American Chemical Society.

7.2. Inductive Hysteresis

The other type of hysteresis is caused by inductive behavior. An inductor with inductance L is described by the equation

$$V = L\frac{dI}{dt} \tag{30}$$

with the correspondent impedance

$$Z = i\omega L \tag{31}$$

The impedance of the basic inductive circuit is shown in **Figure** 18e. The inductance in rectifying nanopores is not of electromagnetic origin but rather corresponds to a general behavior termed the chemical inductor.[45,125] The effective capacitance of the inductor is[125]

$$C^* = -\frac{1}{\omega^2 L} \tag{32}$$

The inductor element is often associated to a "negative capacitance".[126,127] Consequently the direction of inductive hysteresis is reversed with respect to the capacitive hysteresis.

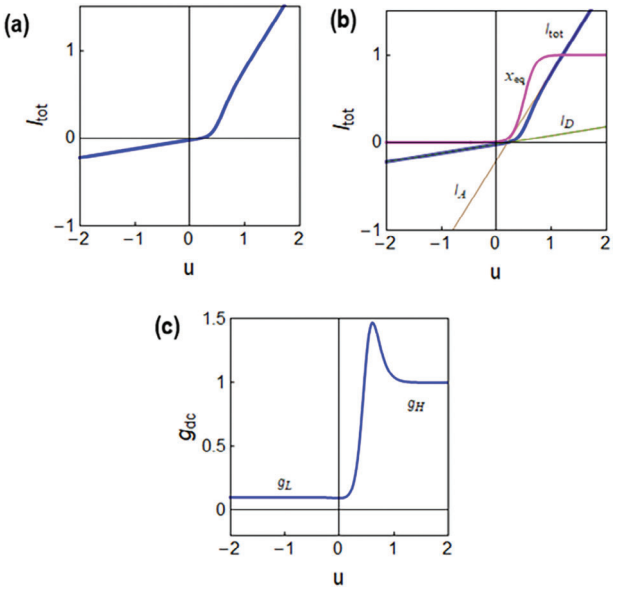

Figure 12. Ionic channel conduction. a) Total current-voltage. b) Components of the current: low conductance current (green), high conductance current (brown), and open channel probability x_{eq} (purple). c) Total resistance. Parameters: $E_0 = 0.2$; $V_B = 0.5$; $V_m = 0.1$; $g_L = 0.1$; $g_H = 1$. Voltage in V and current in μA.

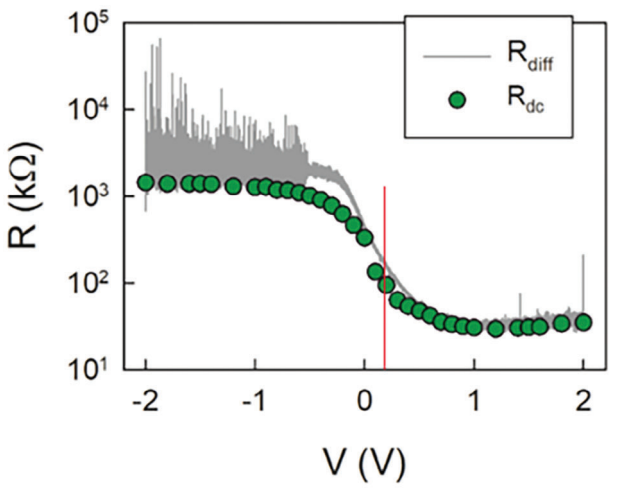

Figure 13. Total resistance of a multipore membrane as in Figure 9 in KCl solution. The calculated value of R_{dc} obtained from impedance data (points) compared to the differential resistance, calculated by the slope of the steady-state current-voltage curve. The red line shows the midpoint of the transition at $V \approx 0.2$ V. Data courtesy of Patricio Ramirez.

This explains the counterclockwise inductive hysteresis loop of Figure 17d.

However, there is a substantial difference between the two types of hysteresis. The capacitive current is an added current, Equation (28), that can be positive or negative. In contrast, the inductive current loops in the models that we discuss here remain roughly between two limits: A slow current, with the maximum conductance g_H, Figure 17d, and a fast current, that has a lower conductance g_L. In inductive hysteresis a forward scan at high velocity reduces the current, because the slow-high current mode is only partially activated.

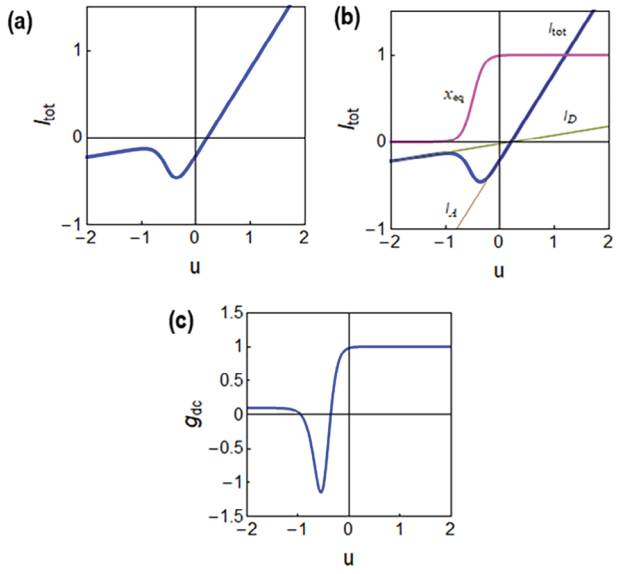

Figure 14. Ionic channel conduction. a) Total current-voltage. b) Components of the current: low conductance current (green), high conductance current (brown), and open channel probability x_{eq} (purple). c) Total conductance. Parameters: $E_0 = 0.2$; $V_B = -0.5$; $V_m = 0.1$; $g_L = 0.1$; $g_H = 1$. Voltage in V and current in μA.

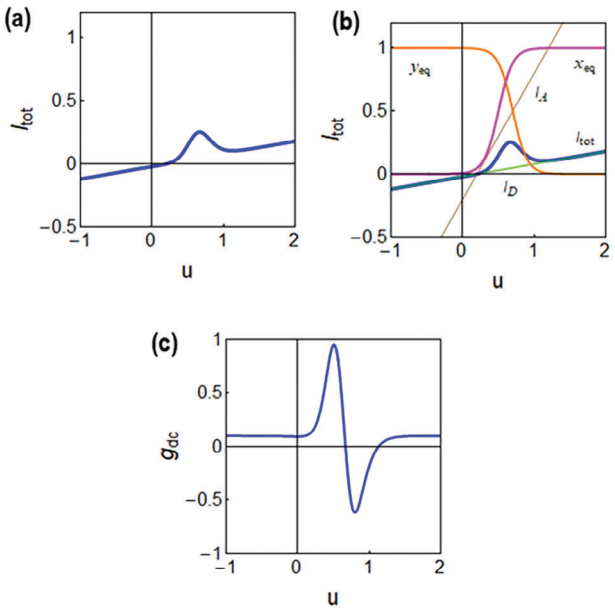

Figure 16. Ionic channel conduction. a) Total current-voltage. b) Components of the current: low conductance current (green), high conductance current (brown), activation variable x_{eq} (purple), deactivation variable y_{eq} (orange). c) Total conductance. Parameters: $E_0 = 0.2$; $V_B = -0.5$; $V_C = 0.7$, $V_m = 0.1$; $g_L = 0.1$; $g_H = 1$. Voltage in V and current in μA.

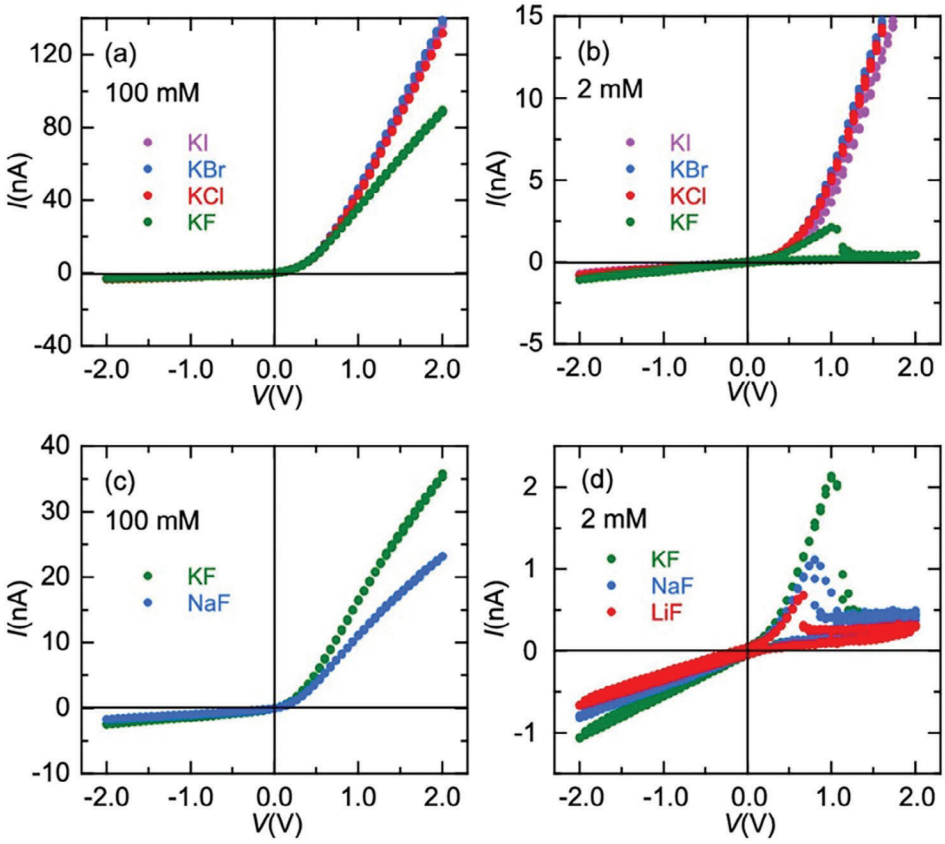

Figure 15. a) I–V curves for multipore polyimide (PI) membranes, in KI, KBr, KCl, and KF at high (100 mM) and b) low (2 mM) concentrations c) I–V curves for NaF and KF at 100 mM and d) LiF, NaF, and KF at 2 mM. Reproduced with permission.[37] Copyright 2024, licensed under a Creative Commons Attribution (CC BY 4.0) license.

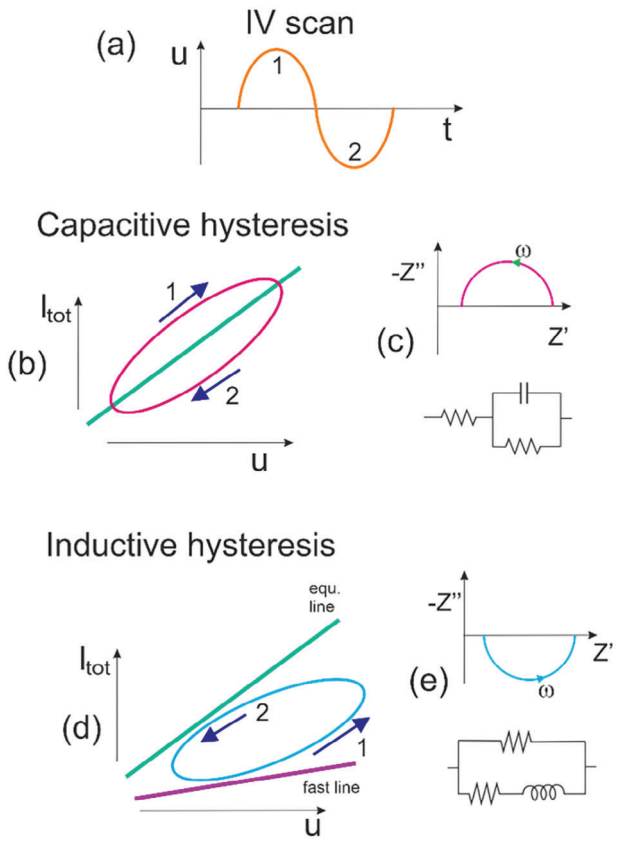

Figure 17. a) Cycle of voltage sweep as Equation (25) with (1) positive (forward) and (2) negative (reverse) velocities. b,d) Current-voltage curves. The green line is the stationary current, the purple line in (d) is the very fast scan limit, and the curved line is the current under the cycle indicated in (a). c,e) Basic impedance spectra and the associated equivalent circuit. The arrow indicates the direction of increasing angular frequency. (b,c) Capacitive system. (d,e) Inductive system.

The two types of hysteresis and the associated impedance spectra are shown in Figure 18 for a conical nanopore.[48] In Figure 18a the nanopore response shows an inductive hysteresis loop at the positive voltage, with the current in the positive sweep being lower than in the negative sweep direction, corroborated by the inductor characteristic at low frequency in the impedance measurements, Figure 18d. Contrarily, in the negative voltage the hysteresis loop is capacitive. The positive sweep current is more positive than the current in the negative direction. This last feature corresponds to the dominant capacitive impedance in Figure 18b. We remark that these measurements confirm the classification obtained in Figure 17.[45]

Remarkably, by changing the pH of the solution the polarity of the nanopores can be inverted, so that the rectification and inductive property can be switched in the voltage axis, as shown in **Figure 19**a,c.[30]

7.3. Crossing or not Crossing Hysteresis Loops

A distinction of current-voltage curves that are self-crossing or not has been remarked.[16,62] These are usually denoted bipolar and unipolar devices. We can interpret such features using root dynamical properties of the system, that determine the hysteresis behavior.

Due to the transition from inductive to capacitive hysteresis, with oppositely spinning currents, the characteristic *IV* curves in Figures 9, 18, and 19, necessary cross at some point close to the origin. This situation is found also in most of the rectifying cylindrical pores reported.[9,35,41,106,107,128] Therefore, self-crossing current-voltage dynamic characteristics indicate a transition from capacitive to inductive hysteresis, or vice versa.[45,129]

Going back to Figure 18, we remark that the transformation of the impedance spectra from capacitance to inductor at low frequency, is indeed obtained when the impedance is measured in a voltage range across the crossing point of the current-voltage curve, when the hysteresis change occurs.[68]

However, in **Figure 20** a different type is shown.[130] This is a regular cylindrical pore, where no rectification occurs. The hysteresis is capacitive at both sides of voltage, hence no crossing of the *IV* curve happens.[131]

8. Hysteresis in Nanopores

To obtain the hysteresis effects we extend the model of Equation (18) to include the kinetic effects. The channel conductance activation, x, is time delayed with respect to the application of the voltage. The reference model for this physical behavior is obtained by two dominant features of the HH[10] model.

First, the blocking variable x is not a direct function of voltage, and Equation (18) becomes

$$I_{tot}(u) = \left[g_L + \left(g_H - g_L\right) x\right] \left(u - E_0\right) \tag{33}$$

Second, the evolution of x is determined by a dynamical equation of the type (2–4), namely

$$\tau_k(u) \frac{dx}{dt} = x_{eq}(u) - x \tag{34}$$

Therefore, in equilibrium $x \to x_{eq}$ recovering Equation (18). The $\tau_k(u)$ is the relaxation time further discussed in Section 10.

The HH-inspired model formed by Equations (33–34), is the essential form of a chemical inductor[125] and also the typical description of a memristor.[60,67] As discussed recently,[45] models of the type (33-34) describe well the main trends of hysteresis summarized in Figure 17 and measured in many conducting systems. With additional dynamical effects (including a negative resistance) the model (33-34) can be developed to make spiking neuron devices.[17,49]

Here we show in **Figure 21** the properties of hysteresis of the model (33-34) using a constant relaxation time τ_0 and a cycling frequency $f_\Omega = \Omega_s/2\pi$. At slow frequencies in panels (a, b, c) the current-voltage follows the shape of the equilibrium curve of Figure 12a, with some opening towards lower current (in the positive voltage side). The separation from equilibrium is inductive at positive voltage to the crossing point, that occurs at $u = E_0$. The hysteresis is capacitive at negative voltages with respect to this point, see the arrows in Figure 21c. The origin of inductive and capacitive contributions to the impedance has been explained by the calculation of the equivalent circuit associated to Equations (33–34).[68]

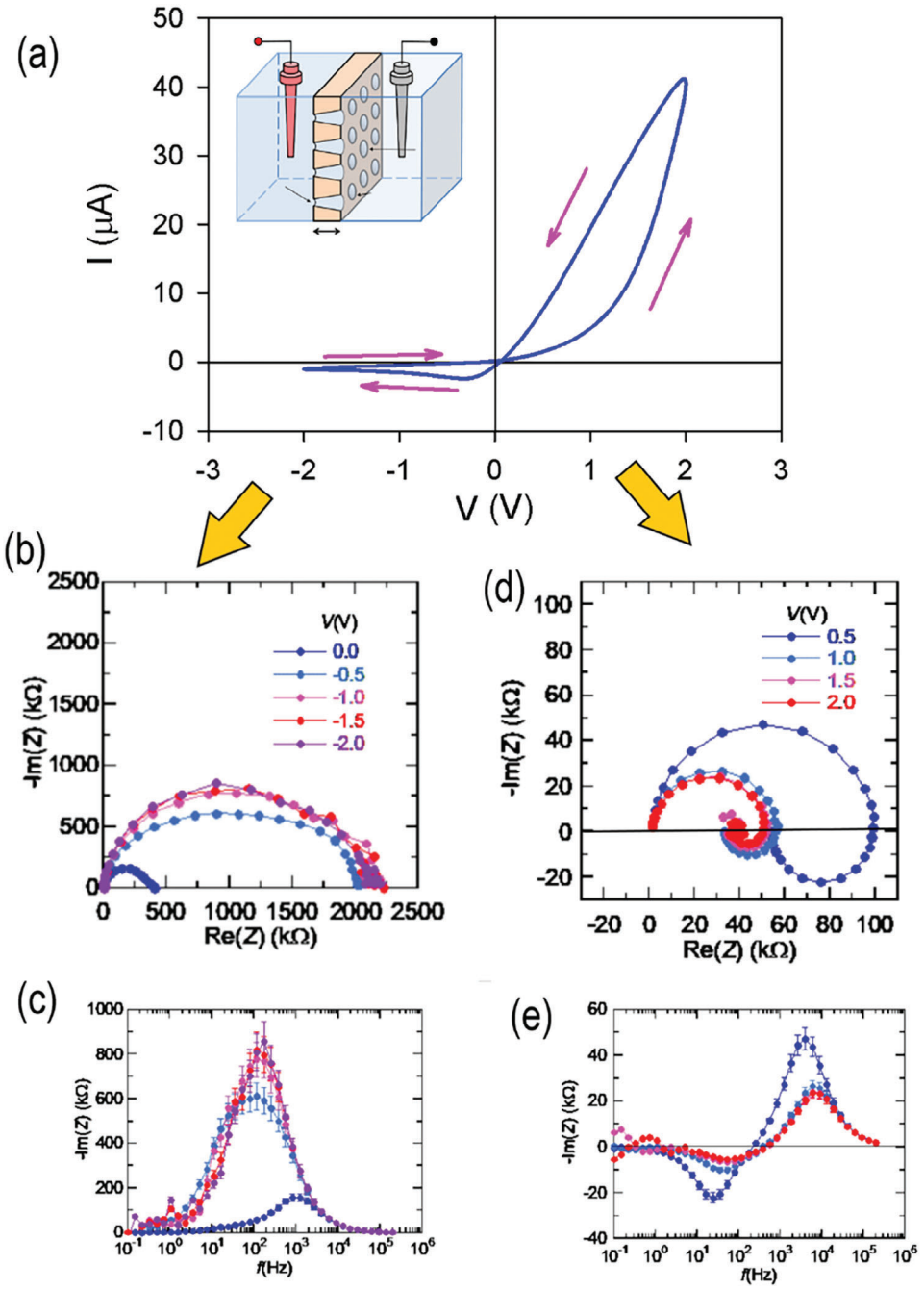

Figure 18. a) Current-voltage curve measured at a frequency of f_Ω = 10 Hz for a multipore membrane in 100 mM KCl solution at neutral pH. The inset shows the electrochemical cell with the membrane. b) The impedance spectra at different reverse voltages, with the corresponding bode plot of the imaginary part of the impedance in (c). d,e) are the impedance spectra and bode plots at forward voltage. Reproduced with permission.[48] Copyright 2024, Elsevier.

Figure 21b–e show that the conductance of the positive lobe progressively descends at larger cycling frequency, as observed in Figure 9a. This property is a central factor to emulation of the natural synapses that show frequency-dependent stimulation in learning tasks.[132,133] At frequency close to $1/\tau_0$, (d, e), the state variable x is unable to reach the value 1, and the conductance cannot arrive to the high value g_H. At very high frequency, (f, g), only the g_L conduction branch (purple line) is active at both negative and positive potentials. We can observe that hysteresis measured by the opening of the curve disappears at these frequencies.

In summary, hysteresis is a transient effect, that increases when the velocity or frequency of the voltage sweep increases. The high conductance component of the current may be lost, as the slow response of the phenomena that causes the

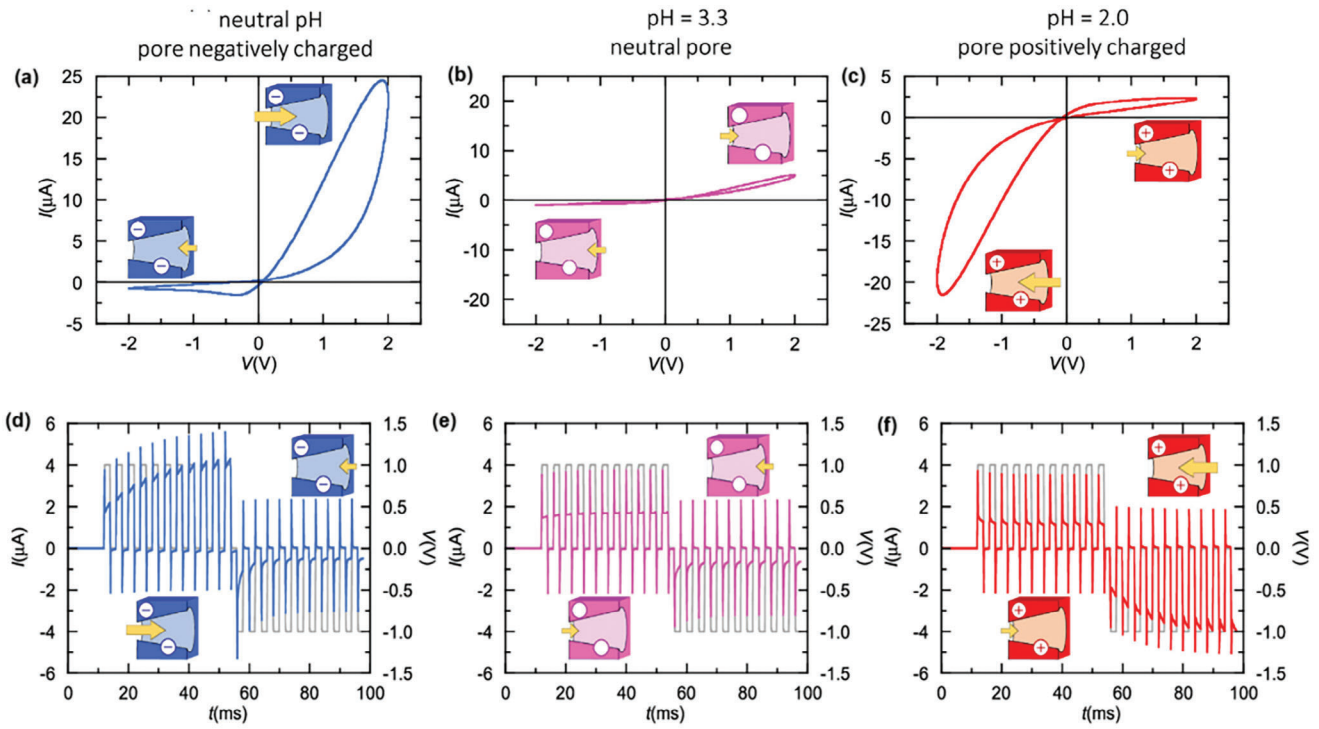

Figure 19. I–V curves for a multipore membrane in 50 mM KCl solution, measured at frequency $f = \Omega_s/2\pi = 10$ Hz. a) I–V curve for a neutral pH solution (negatively charged pore, inset). b) I–V curve for pH = 3.3 (neutral pore, except for a small residual charge) c) I–V curve for pH = 2.0 (positively charged pore). d) Current response (left) to a sequence of 2 ms positive voltage pulses (right) showing a gradual conductance potentiation followed by a sequence of negative voltage pulses, which reset the multipore membrane to the low conductance state for neutral pH. e) Same experiment except for pH = 3.3. f) Same experiment except for pH = 2.0. In all cases, $V_0 = 1$ V and c = 50 mM KCl. Reproduced with permission.[30] Copyright 2023, American Chemical Society.

inductive hysteresis suppresses this part with respect to the stationary response. Relative hysteresis may be reduced at high frequency, as shown in Figure 21e,f.[45,134] It is important to recognize that hysteresis does not require rectification, as we have illustrated in Figure 20.

9. Resistive Switching

Another important property for memory and computing circuits is *resistive switching*.[62,135] This property consists on the change of the system from a high resistance state (HRS) to a low resistance state (LRS) in a SET process. The system can be reverted to the HRS in a RESET process, as shown in **Figure 22**. But before going to the RESET voltage, the system can be operated in the LRS and maintains the property, as indicated in the processes 2–3 in Figure 22, with a long retention time.

The resistive switching has been known for centuries and is often caused by a phase transition, or the forming of a conducting filament in an insulator medium, that creates a nonvolatile conduction pathway, persisting even if the forming voltage is removed.[6,7,135] This behavior corresponds to a bistable system, in which two distinct metastable states can exist at the same voltage. In fact in the normal usage of "memristor" in solid-state devices, the phenomenon of resistive switching is understood, and many authors reserve this denomination for devices that show permanent, non-volatile distinct resistive states.[61] The retention time of an activated state is the parameter determining nonvolatile behaviour.[136]

In contrast to these permanent resistive changes, systems that show only dynamic hysteresis will loose the distinction of a HRS and a LRS if operated slowly, and they are volatile. Rectification, as in Figure 12, and hysteresis, as in Figure 21, do not imply nonvolatile resistive switching.

To the best of my knowledge, all the artificial rectifying nanopores reported in the literature and cited in this work show hysteresis but not nonvolatile resistive switching; they are volatile, with short retention times. Still, volatile memristive systems may be useful for bio-inspired computation.[137]

10. Transition Rates and Relaxation Times

In Equation (34) $\tau_k(u)$ is the relaxation time of the activation of the state variable x. The relaxation time is an important feature controlling the kinetic features of HH models,[11,13] as shown before in Subsection 3.1. The relaxation time also determines the switching and volatility properties in solid-state memristors,[64,66,120] establishing the retention time of the activated state.

To investigate the physical meaning of the relaxation time we formulate another version of the memory Equation (34). The state variable x is regarded as a fractional occupancy of a conducting state, with equilibrium form x_{eq} as in Equation (21). The

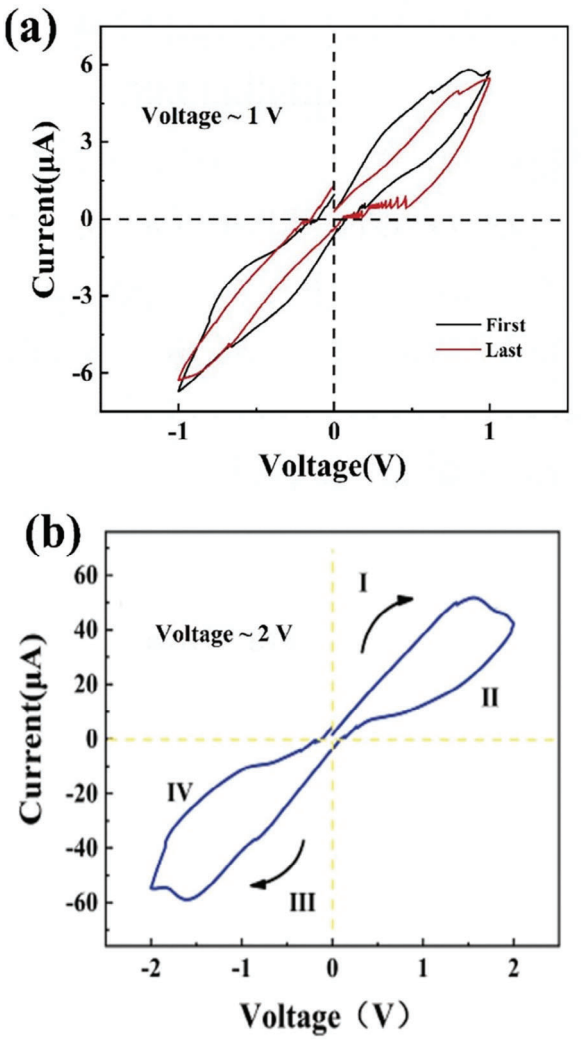

Figure 20. Current-voltage curve of a symmetric quartz capillary with 100 μm inner diameter, and ionic liquid of 1,3-dimethylimidazole chloride salt ($C_5H_9N_2Cl$) with concentration 0.5 mol L^{-1}. The two panels indicate different maximal cycling voltage, as indicated. Reproduced with permission.[130] Copyright 2023, American Chemical Society.

dynamical equation can be presented as a standard master equation in a two-state model[84]

$$\frac{dx}{dt} = \alpha_\tau\ (1-x) - \beta_\tau x \tag{35}$$

The α_τ and β_τ are the rates of creation and destruction of particles, respectively, in the available sites, as in Equations (6–8). In equilibrium we have from (21)

$$x_{eq} = \frac{\alpha_\tau}{\alpha_\tau + \beta_\tau} = \frac{1}{1 + e^{-(u-V_B)/V_m}} \tag{36}$$

We obtain the detailed balance condition[109]

$$\frac{\alpha_\tau}{\beta_\tau} = e^{(u-V_B)/V_m} \tag{37}$$

In general, comparing Equations (35) and (34), it follows that the relaxation time is

$$\tau_k\ (u) = \frac{1}{\alpha_\tau + \beta_\tau} \tag{38}$$

as indicated in Equation (17).

The transition rates can be written in terms of activation and deactivation times, $\tau_A(u)$, $\tau_D(u)$, as follows

$$\tau_A\ (u) = \frac{1}{\alpha_\tau} \tag{39}$$

$$\tau_D\ (u) = \frac{1}{\beta_\tau} \tag{40}$$

Then we have

$$\frac{\tau_D}{\tau_A} = \frac{x_{eq}}{1-x_{eq}} = e^{(u-V_B)/V_m} \tag{41}$$

$$\tau_A\ (u) = \frac{\tau_k\,(u)}{x_{eq}} \tag{42}$$

$$\tau_D\ (u) = \frac{\tau_k\,(u)}{1-x_{eq}} \tag{43}$$

Hence Equation (35) becomes

$$\frac{dx}{dt} = \frac{(1-x)}{\tau_A\,(u)} - \frac{x}{\tau_D\,(u)} \tag{44}$$

And the full relaxation time of Equation (34) is

$$\tau_k\,(u) = \left(\frac{1}{\tau_A} + \frac{1}{\tau_D}\right)^{-1} \tag{45}$$

There are many possible ways to formulate Equation (45) compatible with Equation (41), corresponding to the different selections of the transition rates. For example, for a constant relaxation time model of Figure 21 one has simply $\alpha_\tau = x_{eq}\,/\tau_0$.

However, we expect that nontrivial kinetics of the gating variable will produce variable relaxation times. The analysis of HH model in Figure 6f,g, Figure 7, and Figure 8 shows that realistic relaxation times show a peaked shape, with exponential dependencies at both activation and deactivation side, and tending to a constant value at large voltages.

In solid state memristors, the electrochemical processes for filament formation, including nucleation, charge transfer, and mixed charge/ion drift, produces non-linear exponential voltage-time relationship.[138] An overview of the switching dependence on voltage in solid state memristors is shown in **Figure 23** for a variety of Conductive Bridging Random Access Memory (CBRAM) devices.[139] The figure shows an exponential relationship between the time required to switch the device and the applied pulse amplitude. The exponential form is well established in two-terminal resistance switches based on ionic motion,[2,135,140] corresponding to the electrochemical behavior of the switching process.[138] The decreasing relaxation time has been observed in halide perovskite single crystal memristors.[141]

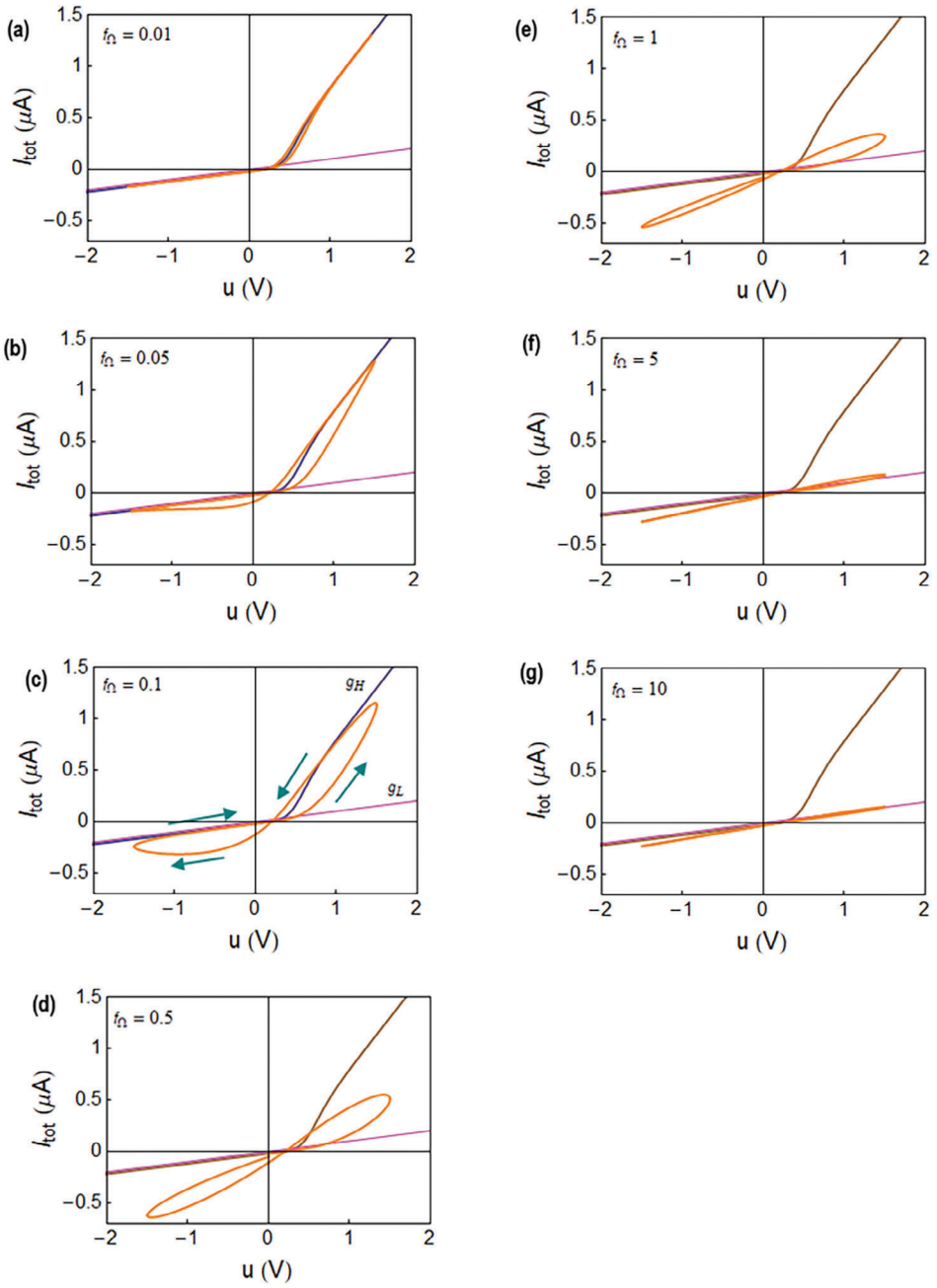

Figure 21. Equilibrium current-voltage (brown), fast current component (purple) and hysteresis current. The cycling frequency f_Ω varies as indicated. Parameters: $E_0 = 0.2$; $V_T = 0.5$; $V_T = 0.1$; $g_L = 0.1$; $g_H = 1$; $\tau_0 = 1$. Voltage in V, current in μA, time in s, and frequency in Hz.

11. A Dynamical Model for Hysteresis in Fluidic Nanochannels

The relaxation times of ionic nanochannels are an essential feature for the neuromorphic behavior of these systems. There is no systematic investigation of the relaxation times of artificial nanopores channels, to my knowledge. Therefore, we build a model based on the properties of natural ion channels and solid-state memristors that we have reviewed in the previous section.[66,68]

11.1. Form of the Relaxation Time

For the analysis of dynamical effects in ionic nanopores, we assume the exponential form of the activation time

$$\tau_A = \tau_0 \, e^{-\frac{u-V_A}{n_A V_m}} \tag{46}$$

with onset parameter V_A and ideality factor n_A. Correspondingly the deactivation relaxation time is

$$\tau_D = \tau_0 \, e^{\frac{u-V_D}{n_D V_m}} \tag{47}$$

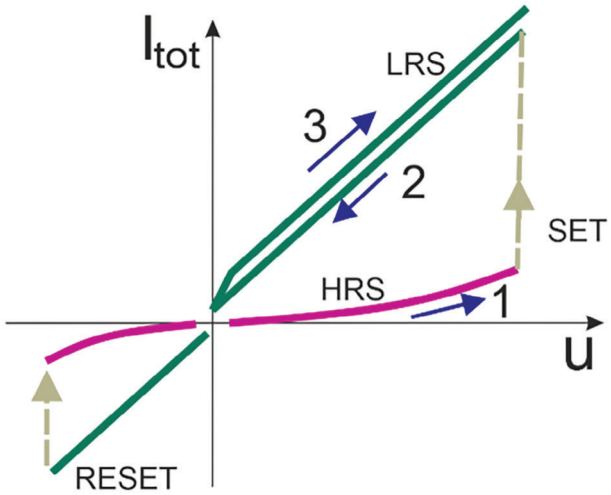

Figure 22. In resistive switching, the system has distinct states of conductivity, a high resistance state (HRS) that can make a transition to a low resistance state (LRS) in a SET process. Once it is in the non-volatile LRS, the voltage can be cycled as in 2, 3 (the two green lines are the same, and separated for ease of visualization). The system can be turned again to the LRS in a RESET process at the complementary polarity.

with parameter V_D and ideality factor n_D. Note that the rise of the state variable x_{eq} in Equation (36) is determined by the parameters V_B, V_m. The consistency with the detailed balance condition (37) requires that the following identities are satisfied

$$\frac{1}{n_A} + \frac{1}{n_D} = 1 \tag{48}$$

$$V_B = \frac{V_A}{n_A} + \frac{V_D}{n_D} \tag{49}$$

The total relaxation time is

$$\tau_k = \tau_0 \left(e^{\frac{u-V_A}{n_A V_m}} + e^{\frac{u-V_D}{n_D V_m}} \right)^{-1} \tag{50}$$

The parameters n_A, n_D enable different slopes in the two voltage wings of τ_k, as observed experimentally in Figure 6f,g and Figure 7. The form of the relaxation time of Equations (50) is illustrated in **Figure 24**. Note that the transition of the gating variable x_{eq} and the maximum of the relaxation time τ_k occur both at the same voltage, V_B.

11.2. Switching Times

In the very origin of the conception of the HH model the transient current in response to a voltage pulse played a protagonist role. Hodgkin and Huxley[10] found very different forms of short and long time behavior of transient curves: a simple exponential decay in repolarization, but a delayed increase in depolarization. They proposed that the potassium conductance is proportional to a power of a variable that obeys a first-order equation, Equations (1) and (4). The transient ionic currents of biological neurons have been amply investigated to elucidate the origin of spiking effects.[11,13] **Figure 25** shows that the analysis of current-voltage curves and voltage-clamp transients enables to determine spiking and bursting patterns in neurons.[142] Some studies show that the transients are useful to investigate the current gating mechanisms of nanofluidic channels.[143]

We investigate the response of the rectifying nanopore to a voltage step from V_0 to $V_0 + \Delta V$. The time dependent applied voltage is

$$V_{app}\ (t) = V_0 + \Delta V\ \theta\left(t - t_0\right) \tag{51}$$

in terms of the unit step function. We calculate the transient current by the Equations (33), (34), and (50). We also consider

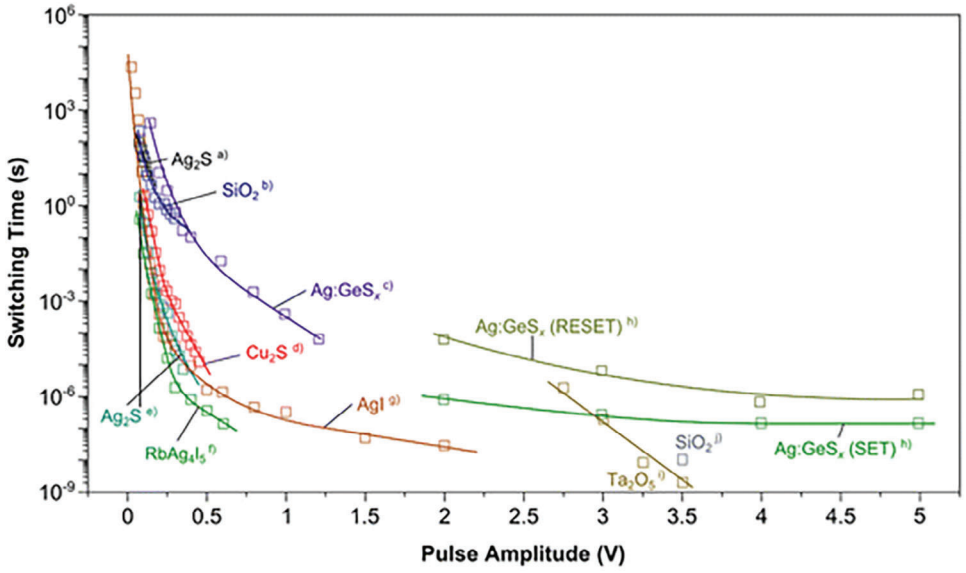

Figure 23. Switching time versus pulse amplitude of several CBRAM devices. Reproduced with permission.[139] Copyright 2017, Springer Nature.

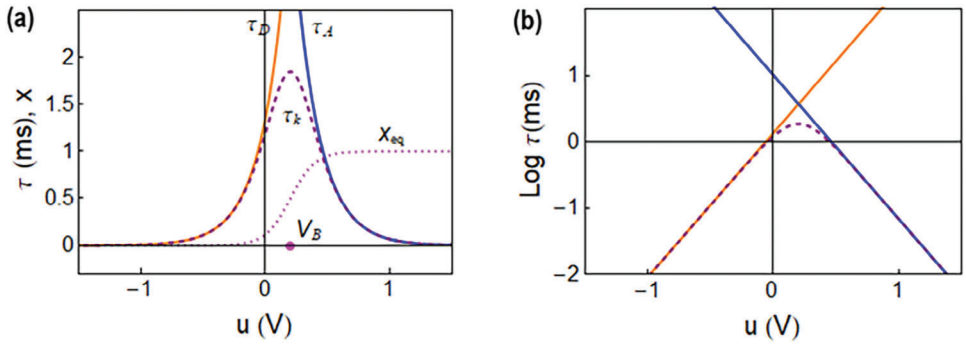

Figure 24. The relaxation time and the equilibrium state variable x_{eq}. The blue line is τ_A, the orange line is τ_D, and the dashed line is τ_k. At the right is shown in semilog representation. Parameters $V_m = 0.1$, $V_B = 0.2$, $V_A = 0.6$, $V_D = -0.2$, $n_A = n_D = 2$, $\tau_0 = 0.5$ *ms*.

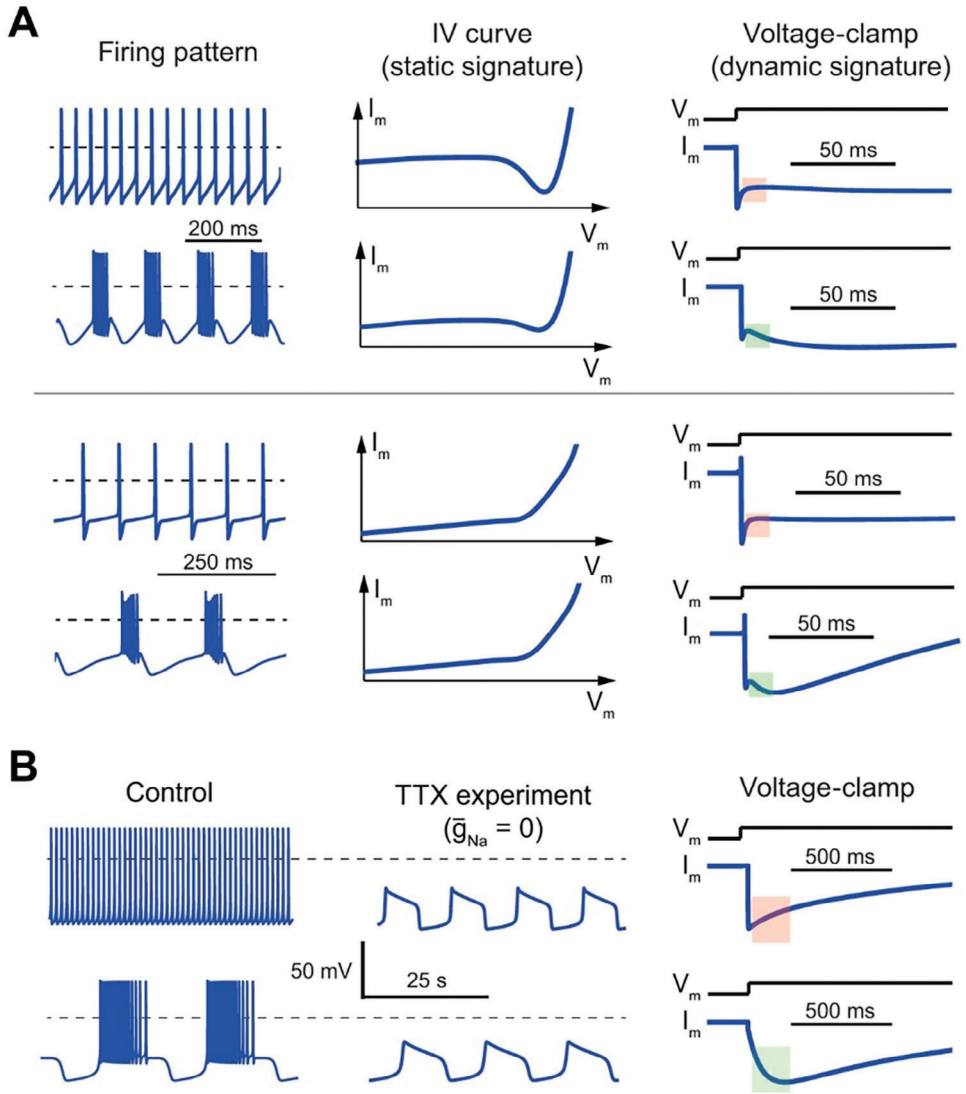

Figure 25. A: a region of negative conductance in the I-V curve is neither necessary nor sufficient for bursting. B: slow oscillatory potentials in the absence of sodium do not necessarily discriminate between fast and slow negative conductances. The Plant R15 Aplysia model exhibits slow oscillatory potential under blockade of sodium channels both in tonic (top) and burst (bottom) modes. Reproduced with permission.[142] Copyright 2017, American Physiological Society.

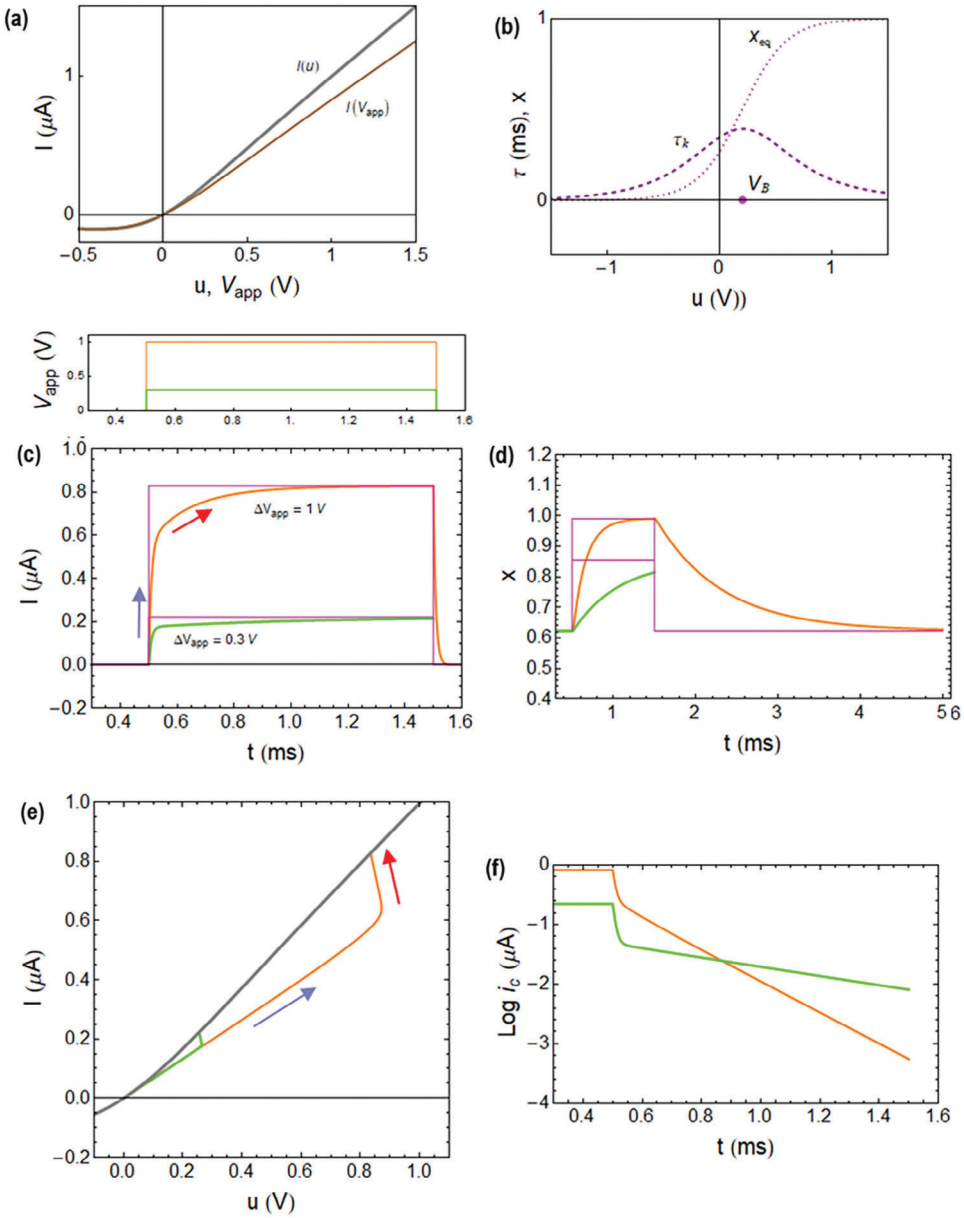

Figure 26. Voltage switching response of the model. a) Current-voltage response with respect to internal (u) and total (V_{app}) voltage. b) Relaxation time and gating variable. c) Current transients. The orange and green lines indicate internal current$[g_L + x(g_H - g_L)]u$. The magenta line is the final equilibrium current. The arrows indicate the progression of fast and slow components. d) Internal variable. e) Evolution of the transients in current-voltage curve. (f) Normalized current dependence on time. Parameters $g_L = 0.1$, $g_H = 1$, $g_s = 5$, $C_m = 0.05$, $V_m = 0.2$, $V_B = -0.1$, $V_A = 0.1$, $V_D = -0.3$, $n_A = n_D = 2$, $\tau_0 = 1$. Time in ms, current in μA.

a series resistance with a conductance g_s, so that the applied voltage is divided as

$$V_{app} = I_{tot}/g_s + u \tag{52}$$

We include a capacitive current added to (33) due to the nanoporous membrane static capacitance,

$$I_{cap} = C_m \frac{du}{dt} \tag{53}$$

The results of the transients are shown in **Figure 26**. Figure 26a,b shows the current-voltage and the relaxation time of the model. Figure 26c shows the transient current from $V_0 = 0$ to two different final voltage values. Here we represent the internal current $[g_L + x(g_H - g_L)]u$. The current shows two domains: a very rapid initial rise (purple arrow), and a subsequent slower rise (red arrow) to the final equilibrium value imposed by the voltage. The two domains are well separated in the IV plane in Figure 26e. The first rapid rise, corresponds to a fast linear increase of the voltage in IV plane, and includes the capacitive peak discussed later. In

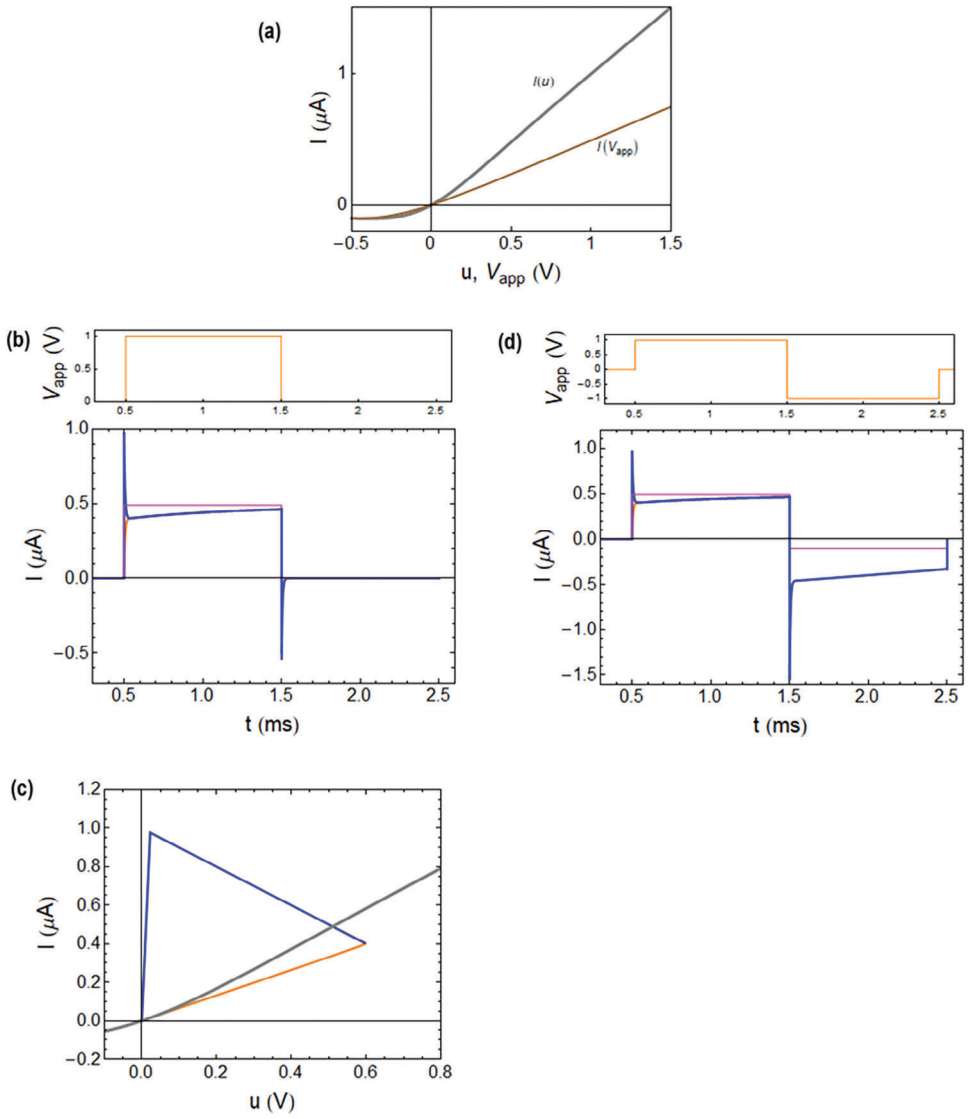

Figure 27. Voltage switching response of the model. a) Current-voltage response with respect to internal (u) and total (V_{app}) voltage. b) Current transients. The blue line is the total current and the orange line indicates internal current $[g_L + x(g_H - g_L)]u$. The magenta line is the final equilibrium current. c) Evolution of the transients in current-voltage curve for case (b). d) Transient current for positive and negative voltage pulses. Parameters $g_L = 0.1$, $g_H = 1$, $g_s = 1$, $C_m = 0.01$, $V_m = 0.2$, $V_B = -0.1$, $V_A = 0.1$, $V_D = -0.3$, $n_A = n_D = 2$, $\tau_0 = 1$. Time in ms, current in μA.

this time lapse the current is due to the initial value of the gating variable that exists at the starting voltage, $x_0 = x_{eq}(V_0)$, that is observed in Figure 26d, with a partial conductance $[g_L + x_0(g_H - g_L)]$. Then the x increases until it reaches equilibrium. This nearly exponential domain is governed by the relaxation time at the target voltage $V_0 + \Delta V$. That is why equilibration is much faster at larger voltage.

To better observe the exponential dependence, we plot in Figure 26f the remaining current

$$i_c(t) = I_{dc}(V_0 + \Delta V) - I_{tot}(t) \tag{54}$$

We remark that the current I_{tot} increases exponentially, according to the value of the relaxation time. This observation provides a method to determine experimentally the relaxation time dependence on the voltage.[14] We can also observe in Figure 6d that the return to the initial current upon disconnection is much longer than the rise, due to the longer relaxation time at $V_{app} = 0$.

A popular approach to memristors modeling uses a split of Equation (44) in two simpler separate equations, one for the activation and one for the deactivation side of the voltage axis.[66,120,144–146] This piecewise structure of the model should be applied with care, since a large error is produced if using only τ_A or τ_D in the central domain of voltage in Figure 24a.

Now we consider the full transient response to the step voltage of Equation (51), including the capacitive current due to the constant capacitance C_m. The total current is shown in blue line in **Figure 27**, and the main feature with respect to the

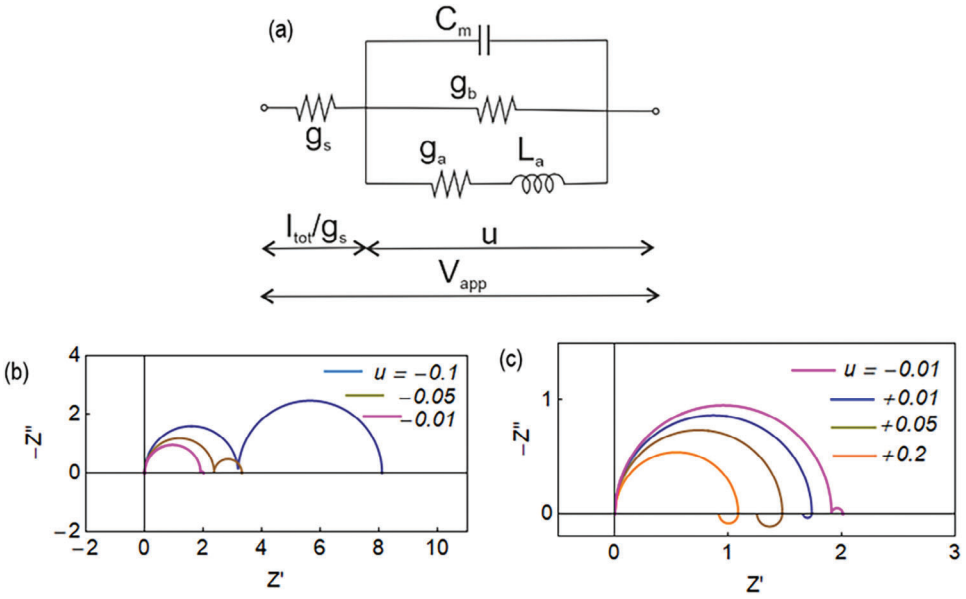

Figure 28. a) Equivalent circuit with conductances g_s, g_a, g_b, capacitance C_m and inductor L_a, indicating the distribution of the applied potential. b, c) Impedance spectra of the model at different stationary voltages. Parameters $V_A = 0.3$, $V_D = -0.4$, $V_m = 0.1$, $n_A = 1.5$, $n_D = 2$, $g_L = 0.1$, $g_H = 1$, $\tau_0 = 1$, $C_m = 0.001$. Reproduced with permission.[68] Copyright 2024, Royal Society of Chemistry.[68]

orange line in Figure 26 is the initial spike when the voltage is connected.

The analysis of the transient is facilitated by the equivalent circuit for small ac impedance of the model, that has been derived in ref. [68] and is shown in **Figure 28a**. The starting current spike in Figure 27b is due to the applied voltage being located in the series resistance (as the capacitor C_m is discharged), therefore the starting current is given by the product $\Delta V g_s$. Then the capacitor is charged and the voltage u increases in the active circuit. The current raises, due to the chemical inductor mechanism, as discussed in Figure 26c. The general pattern is therefore a combination of capacitive (decreasing) current with characteristic time

$$\tau_s = \frac{C_m}{g_s} \tag{55}$$

and inductive (increasing) current with time constant

$$\tau_k = g_a\ L_a \tag{56}$$

Here the inductor relaxation time τ_k is that given in Equation (45).[68]

When the voltage is disconnected in Figure 27b the capacitive peak becomes inverted, since the capacitor is initially charged. These trends have been described for synaptic applications[118] and will be further discussed in the next section.

In Figure 27d shows the transient behavior when the applied voltage is inverted, first with a positive and then a negative pulse. This pattern is used in cycles of potentiation and depression of synapses, see Figure 19d. The current under the positive voltage step has been already discussed. Under a subsequent *negative* voltage the current after the initial spike shows a *decrease*, which is the opposite of the inductor behavior. This in fact observed experimentally for the negative voltage pulses in Figure 19d.

This behavior indicates that the model of Figure 28a generates a variable *capacitance*, in addition to the C_m element in Figure 28a. This remark is confirmed by the calculation of the impedance $Z_a = g_a^{-1} + i\omega L_a$ of the branch (g_a, L_a). The effective capacitance is given by the expression[68]

$$C_a(\omega) = \frac{1}{i\omega\ Z_a} = \frac{g_a}{-\tau_k\omega^2 + i\omega} \tag{57}$$

Therefore

$$Re\ (C_a) = -\frac{g_a\tau_t}{1+\tau_k^2\omega^2} \tag{58}$$

When $g_a > 0$ the system generates the negative capacitance effect associated to the chemical inductor, that is found at positive voltage.[126,127,147–154] The elements g_b and (g_a, L_a) generate the orange line in Figure 26. However, when $V < 0$ it is $g_a < 0$ and the chemical inductor model produces a *positive* low frequency capacitance. These properties are confirmed by the impedance spectra shown in Figure 28b,c. There is a high frequency capacitive arc due to C_m at all voltages. But at low frequencies the behaviour changes from a positive to a negative arc as the voltage changes from negative to positive. These features of the model describe well the experimental observations reported in Figure 18.

11.3. Hysteresis Effects

The properties of hysteresis of rectifying nanopores have been shown in Figure 9. There are two experimental parameters determining the curves, the sweep frequency and voltage amplitude.

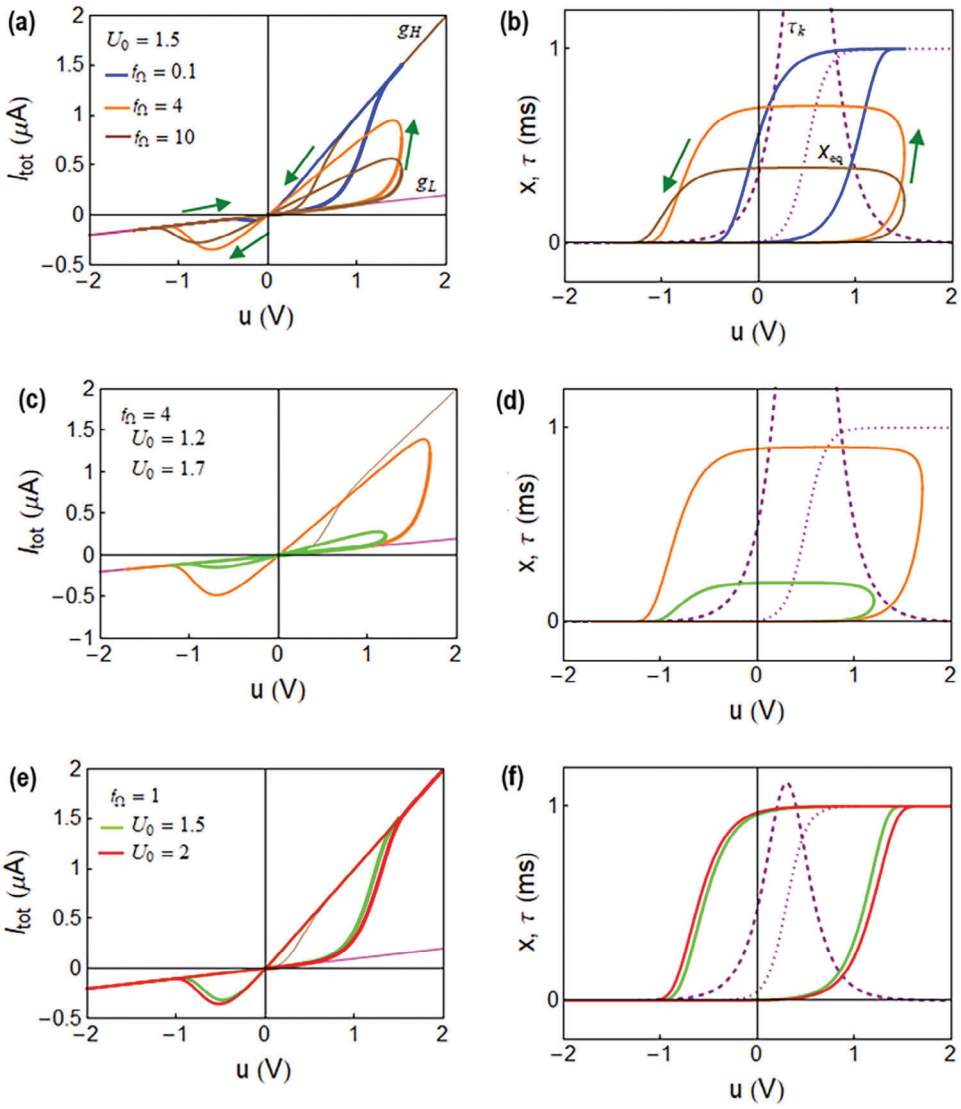

Figure 29. Stable hysteresis current-voltage loops, *x*-variable loops, and relaxation times (purple), at different values of cycling frequency f_Ω and amplitude U_0. g_L is the low conductivity line, and g_H the high conduction branch. Parameters $g_L = 0.1$, $g_H = 1$, $V_m = 0.1$, $\tau_0 = 0.5$, $n_A = n_D = 2$. a–d) $V_B = 0.5$, $V_A = 1$, $V_D = 0$. e,f) $V_B = 0.3$, $V_A = 0.6$, $V_D = 0$. Time in ms, frequency in kHz, current in μA.

The forms of the loops with respect to frequency are already explained by the model of Figure 21, that uses a constant relaxation time. However, the model with the voltage-dependent relaxation time, formed by Equations (33), (34), (50), namely

$$I_{tot}(u) = \left[g_L + \left(g_H - g_L\right) x\right] \left(u - E_0\right) \tag{59}$$

$$\tau_k(u) \frac{dx}{dt} = x_{eq}(u) - x \tag{60}$$

$$\tau_k = \tau_0 \left(e^{\frac{u-V_A}{n_A V_m}} + e^{\frac{u-V_D}{n_D V_m}} \right)^{-1} \tag{61}$$

can explain additional detailed hysteresis properties, and also the synaptical potentiation as discussed later.

We show in **Figure 29** the hysteresis features of the model. Figure 29a,b show the decrease of conductance at higher frequency, as explained before and observed in Figure 9a. Figure 29c,d shows that if we cut the voltage at a lower U_0 amplitude, the onset of the high current state is consequently diminished, as in Figure 9b.[90] Figure 29e,f show the effect of the decrease of the relaxation time at positive potential. When τ_k becomes small at $V \approx V_A$, the hysteresis effect disappears, and the current is reversible and ohmic at high voltage, following the g_H line. Then the hysteresis is not affected by the maximum amplitude of cycling U_0. This feature is also observed in the negative voltage side of all the cases.

To better analyze this property of the capacitive side, we show in **Figure 30** a set of parameters where $g_L > g_H$. The rectification property is inverted, and the high branch occurs at the negative voltages (as in Figures 10 and 19c). Hence in the positive voltage

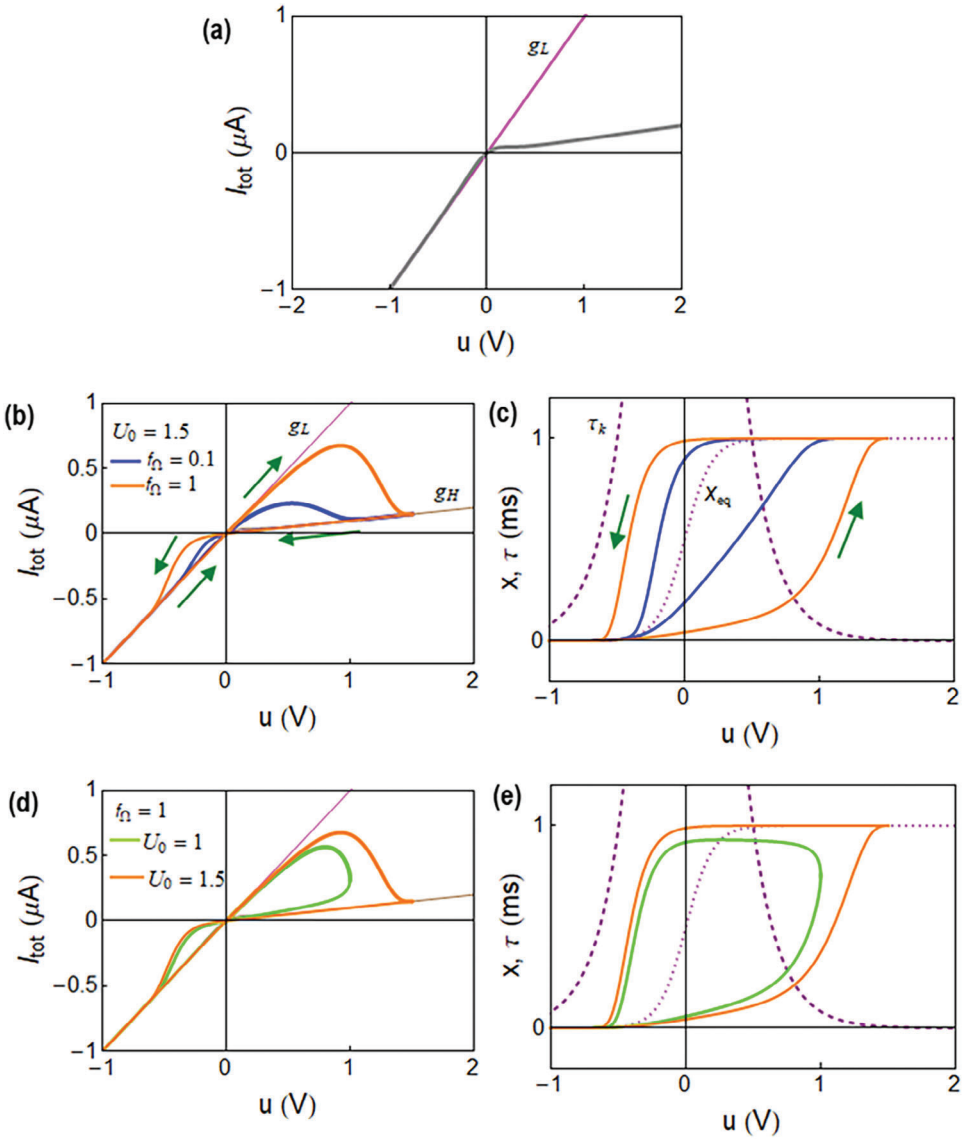

Figure 30. a) Stationary current-voltage curve and b–e) stable hysteresis current-voltage loops, *x*-variable loops, and relaxation times (grey), at different values of cycling frequency f_Ω and amplitude U_0. g_L is the low conductivity line, and g_H the high conduction branch. Parameters $g_L = 1$, $g_H = 1/10$, $V_m = 0.1$, $V_B = 0$, $V_A = 0.5$, $V_D = -0.5$, $\tau_0 = 0.1$, $n_A = n_D = 2$. Time in ms, frequency in kHz, current in μA.

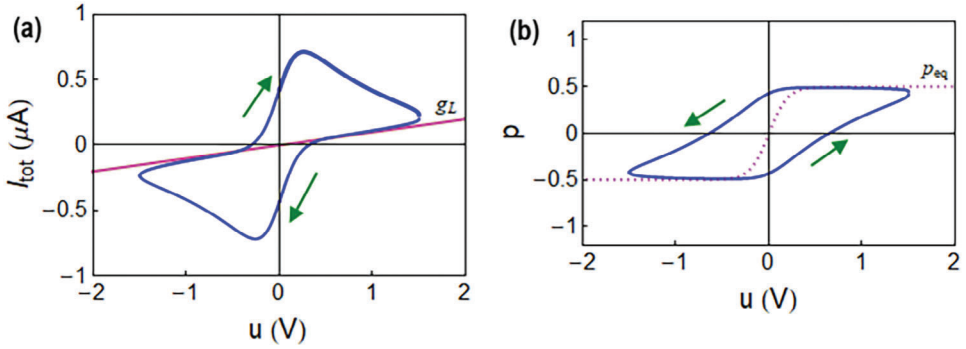

Figure 31. Capacitive model with constant relaxation time τ_0. Hysteresis loops at $U_0 = 1.5$, $f_\Omega = 0.1$. a) current-voltage and b) *p* variable. Parameters $g_L = 0.1$, $E_0 = 0$, $V_m = 0.1$, $V_B = 0$, $\tau_0 = 1$, $p_m = 0.5$, $Q_0 = 1$. Time in ms, frequency in kHz, current in μA.

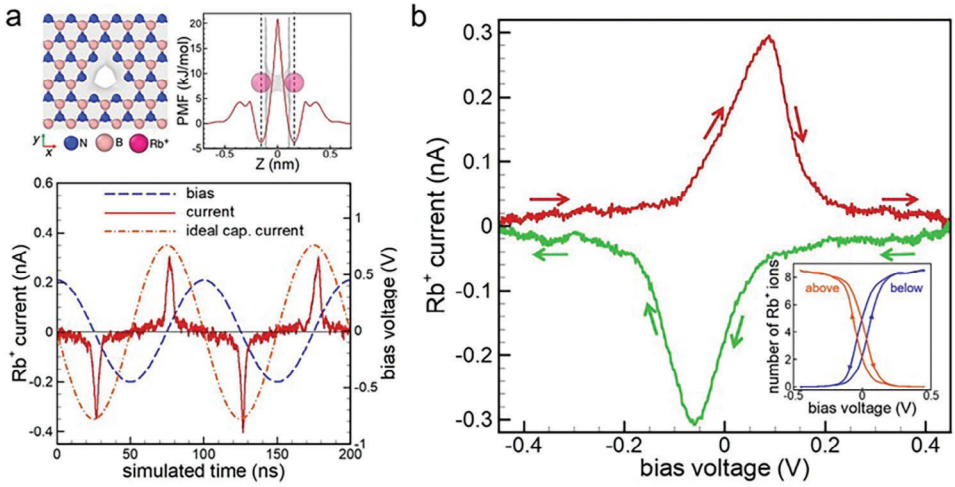

Figure 32. Spiking capacitive Rb^+ currents through subnanometer-porous hexagonal boron nitride. a) Pore structure, the corresponding PMF curve for Rb^+ ions, and the simulated ionic current as a function of simulated time and b) the corresponding Lissajous curve for $U_0 = 0.45$ V and $f_\Omega = 10$ MHz. Reproduced with permission.[131] Copyright 2024, American Chemical Society.

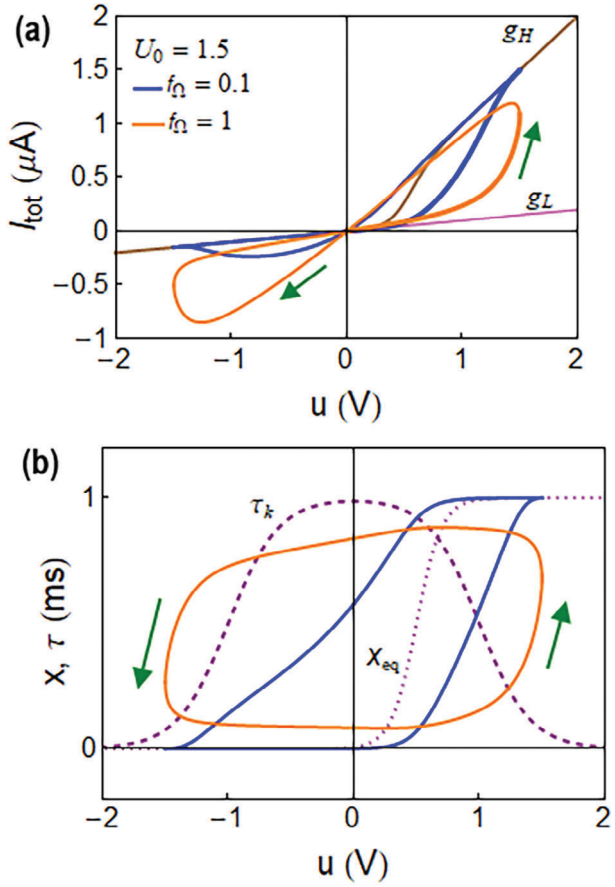

Figure 33. Stable hysteresis current-voltage loops, *x*-variable loops, and relaxation times (grey), at cycling frequency f_Ω and amplitude U_0. g_L is the low conductivity line, and g_H the high conduction branch. Parameters $g_L = 0.1$, $g_H = 1$, $V_m = 0.1$, $\tau_0 = 1$, $\tau_M = 1$, $n_A = n_D = 2$. $V_{Bx} = 0.5$, $V_{B\tau} = 0$, $V_A = 1$, $V_D = -1$. Time in ms, frequency in kHz, current in μA.

side of Figure 30b,d we observe fully the capacitive hysteresis, in which the forward current decreases at some point, according to the frequency and the cycling voltage.

11.4. Capacitive Model

For further insight to the capacitive behavior of Figure 30, we recall that fully capacitive, symmetric, non-crossing loops have been reported as shown in Figure 20. This is not described by the model of Equation (33), that contains a gating voltage. We propose a different approach by the following equations

$$I_{tot}\ (u) = g_L\ (u - E_0) + Q_0 \frac{dp}{dt} \tag{62}$$

$$\tau_k\,(u)\ \frac{dp}{dt} = p_{eq}\ (u) - p \tag{63}$$

$$p_{eq} = \frac{1}{1 + e^{-(u - V_B)/V_m}} - p_m \tag{64}$$

The model is shown in **Figure 31**. The dc conduction is simply ohmic with a single conductance g_L. The state variable p is a polarization variable, and the equilibrium value p_{eq} is fully antisymmetric with respect to voltage for $p_m = 0.5$. As required the capacitive term dp/dt with total charge Q_0 produces non-crossing and symmetric capacitive hysteresis loops. These basic properties are well reproduced in **Figure 32** that shows the detailed molecular dynamics simulation of dynamically biased nanofluidic systems by transport through arrays of graphene-embedded crown pores.[131]

11.5. General Relaxation Time

In the model of Figures 24 and 29, the transition of x_{eq} from 0 to 1, and the maximum of the relaxation time, occur at the same

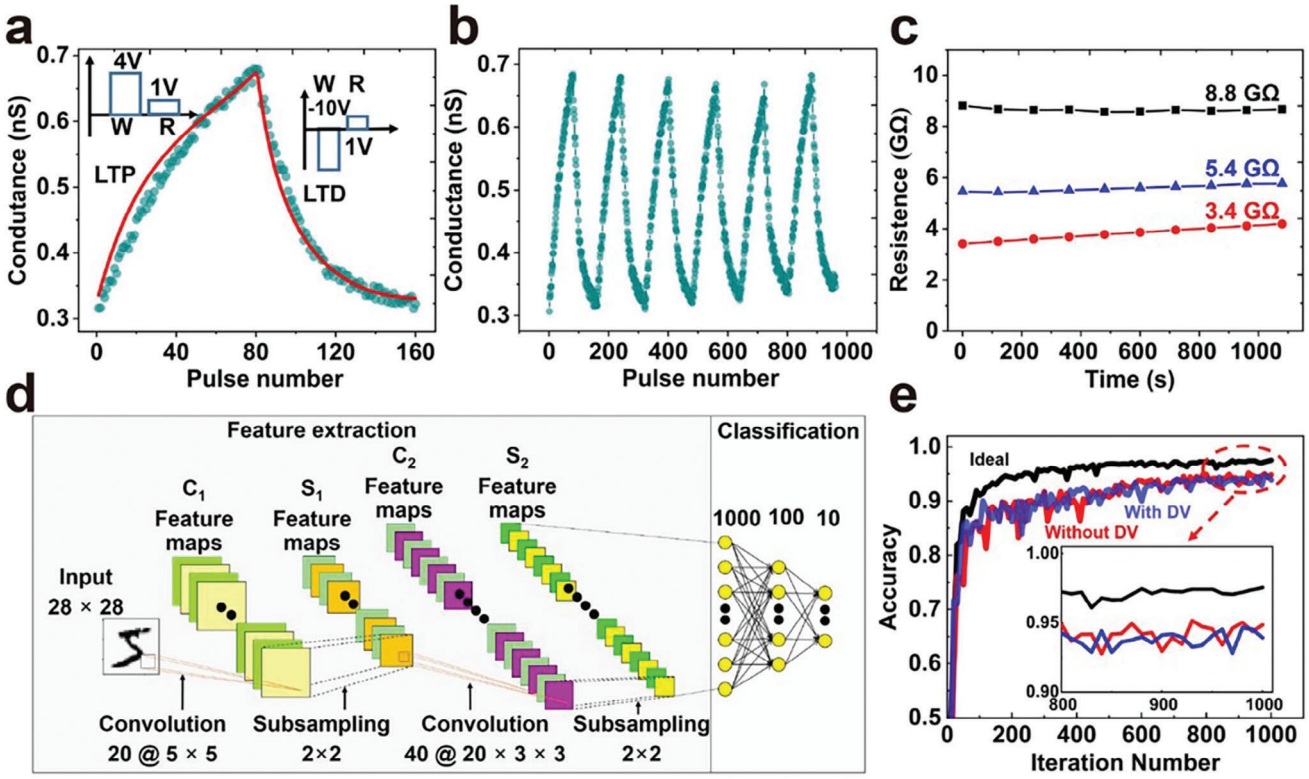

Figure 34. Nanochannel as a synapse and its performance in neural network recognition tasks. a) The analog weight change of nanochannel synapses when a SET pulse train (4 V, 0.5 s, N = 80) followed by a RESET pulse train (−10 V, 0.5 s, N = 80) are imposed on the nanochannel system. Long term potentiation (LTP) and depression (LTD). The dark green dots show the measured conductance after each programmed pulse. b) Endurance: the conductance of the nanofluidic device as a function of the cycle number. c) Retention: three typical states, i.e., an HRS (black line), an LRS (red line), and a midresistance state (blue line), measured every 2 min. d) Schematic diagram of a CNN comprising feature extraction and classification for a handwritten digit-recognition task. Both the convolutional kernels in the feature extraction unit and the connections in the classification unit are simulated by our nanochannel synapses. e) The simulated recognition accuracy as a function of the training time. The black line shows results using the ideal analog behavior of the synapses, whereas the blue and red lines are the results with and without consideration of the device variation. Inset plots show that the accuracy reaches a steady state in the three different situations after 800 iterations. Reproduced with permission.[22] Copyright 2019, American Chemical Society.

voltage, V_B. The activation and deactivation of the hysteresis loops by the reduction of the τ_k occur approximately equally at both sides of the center V_B. We now propose a more general model in which the transition of x_{eq} occurs at V_{Bx} while the peak of the relaxation time is at a voltage $V_{B\tau}$, both parameters being different. In addition, we introduce a cutoff value τ_M to the relaxation time, associated to the maximum velocity of the kinetic relaxation process.

The complete model is formed by the equations.

$$I_{tot}(u) = \left[g_L + \left(g_H - g_L\right) x\right] \left(u - E_0\right) \tag{65}$$

$$\tau_k(u) \frac{dx}{dt} = x_{eq}(u) - x \tag{66}$$

$$x_{eq} = \frac{1}{1 + e^{-\left(u - V_{Bx}\right)/V_m}} \tag{67}$$

$$\frac{1}{\tau_k} = \frac{1}{\tau_M} + \frac{1}{\tau_0}\left(e^{\frac{u - V_A}{n_A V_m}} + e^{-\frac{u - V_D}{n_D V_m}}\right) \tag{68}$$

$$\frac{1}{n_A} + \frac{1}{n_D} = 1 \tag{69}$$

$$V_{B\tau} = \frac{V_A}{n_A} + \frac{V_D}{n_D} \tag{70}$$

Figure 33 shows the new properties, with respect to Figure 29, in which the reset process at negative voltage can occur far from the activation voltage V_{Bx} of the gating variable. These properties are of outmost significance for the operation of neuromorphic circuits.[155] The region where τ_k is high in Figure 33, determines the voltage range where the written ON state persists. The value of τ_k in this region, indicates the retention time, and establishes the volatile operation time.

12. Neuromorphic Applications

The general properties and objectives of neuromorphic circuits have been summarized in Sections 2 and 3. Now we consider the progress reported so far using nanopore ionic channels, and the

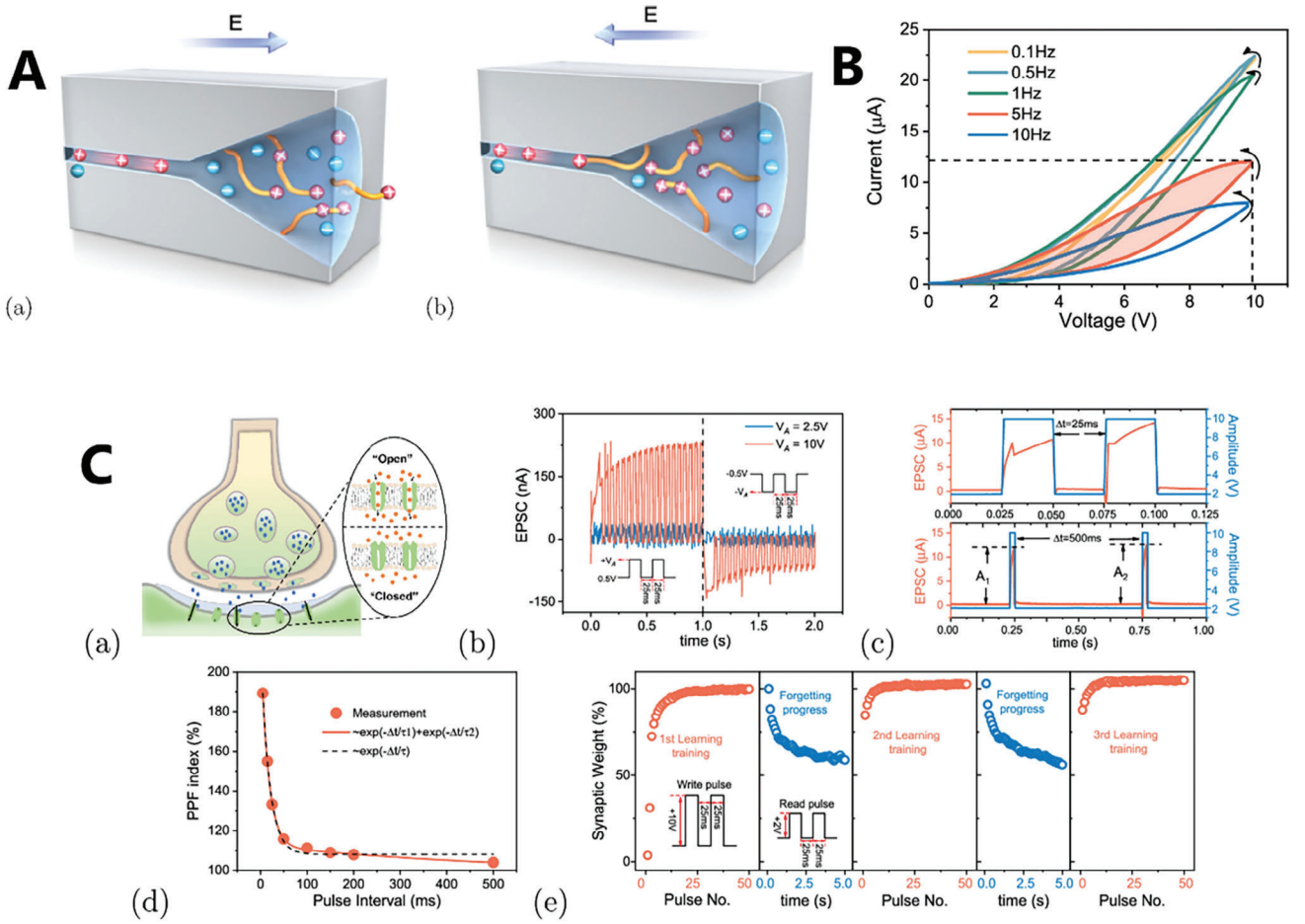

Figure 35. A. a) The positive electric field E drives poly-l-lysine (PLL) molecules out of the channel, inducing resistance decreases as an "open" state. b) Negative E forces the PLL molecules to penetrate into the channel overcoming the entropy barriers, resulting in resistance increases as a "closed" state. The negative charge at the wall of the Angstrom channel represents the surface charge. B. The I–V curves at positive bias voltage in various scanning frequencies with 10 mM KCl solution at pH = 5.0. C. Emulation of synaptic functions in our nanofluidic system. (a) Scheme of a biological synapse. (b) The current amplitude increases as a number of spikes with V_A = 10 V; however, it remained constant with V_A = 2.5 V. c) The current recording with paired-pulse potentiation in various time intervals (Δt) of pulses. d) The factor PPF exponentially decreases as the time interval of pulses. e) The learning-experience behavior of our nanofluidic artificial synapse system. The synaptic weight change increases and saturated after ≈15 potentiation spikes, while it still remained at a certain value and "learned" faster in the next potentiation cycles. All measurements were measured in 10 mM KCl solution with pH = 5.0. Reproduced with permission.[25] Copyright 2023, American Chemical Society.

insights about the experimental results that can be obtained using a phenomenological model that connects the hysteresis and transient behaviors.

For the forming a computational network based on ionic channels, as shown in **Figure 34**d,[22] several factors are to be considered. The elements need to have the synaptical response;[19] they must be combined into functional circuits; and neuron elements are required for obtaining SNN. We consider these elements in turn.

12.1. Rectifying-Inductive Pores for Synapses

For establishing the operation of a neural network, conductance modulation of the synaptic elements is required. This property is achieved by potentiation and depression at successive voltage pulses, as shown in Figure 34a.[22,156] Looking at the current features more closely in **Figure 35**C(b–c),[25] we find the increase of current (or conductance) at positive pulses, and the decrease at negative pulses. These characteristic patterns can be seen more clearly in Figure 19d.

The current response to a voltage pulse can be understood with reference to Figure 27b. It is formed by an initial capacitive spike, and the subsequent gradual increase due to the inductor functionality. The inductor, generally represented by the model with two conductance states and a gating variable, is therefore the fundamental property for potentiation behavior. As we have mentioned earlier, the inductive property is readily revealed by impedance spectroscopy measurement, see Figures 11, 18 and 28.

Upon reversal of the voltage sign (negative voltage pulses) in Figure 19d, the current decreases in successive pulses. As we

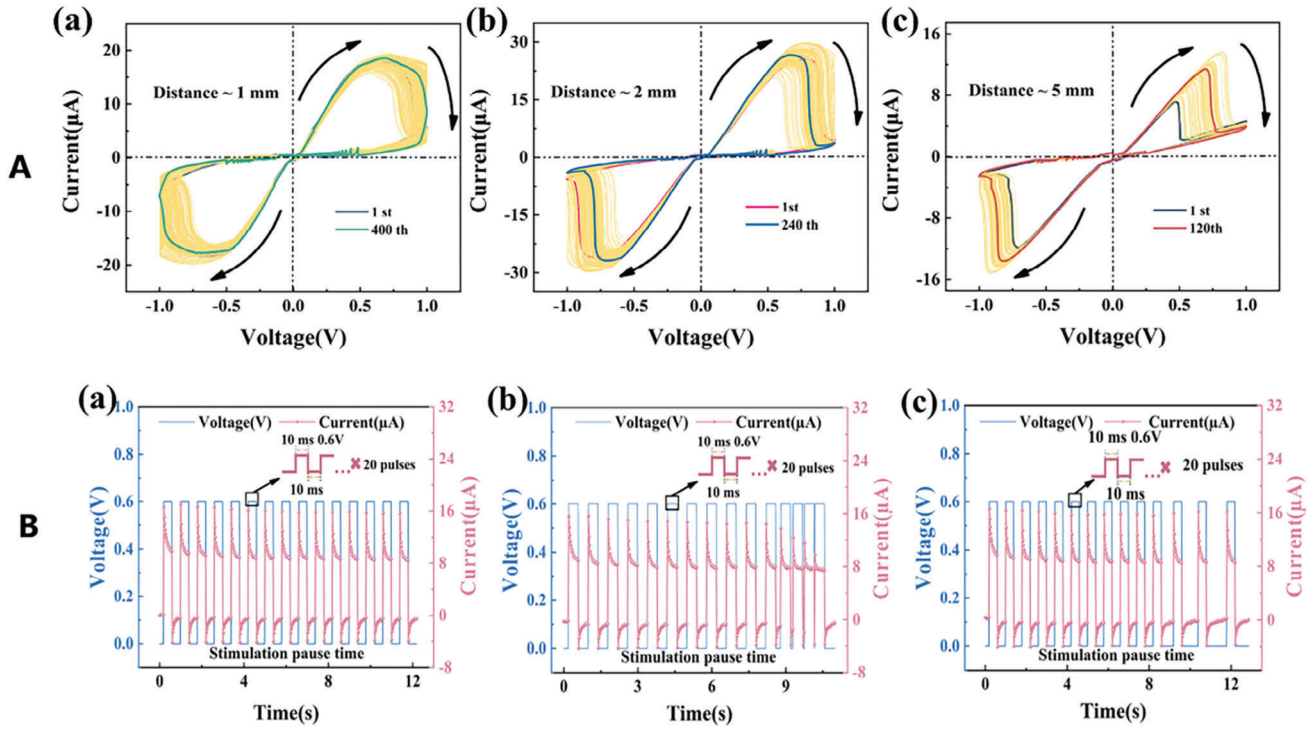

Figure 36. A. Microfluidic memristors with different spacing of electrodes: a) 1 mm, b) 2 mm, and c) 5 mm, the corresponding cycle number and durability of HRS and LRS with different electrode distances. B. Three modes of gap times between each adjacent set of stimuli: (a) constant, (b) shrinking, and (c) growing gap, respectively, with a pulse amplitude of 0.6 V including 20 stimuli each set.[158] Reproduced with permission,[158] licensed under a Creative Commons Attribution (CC BY 4.0) license.

have commented in Figure 27d, here the voltage is in a capacitive domain, thus the current cannot increase. Note in Figure 19f that the potentiation (increasing current) occurs at negative voltage, since the high current has been voltage-inverted in this sample. We also remark that the current increases from one pulse to the other. The synaptic behavior of pore channels is fully described in a separate publication.[157]

12.2. Capacitive Pores

As we have commented in several examples, capacitive pores without rectification and without self crossing have also been described, Figure 20 and Figure 32. Another example is shown in **Figure 36**A. We observe that the hysteresis curves have the general shape of Figure 31, although for longer pores (b,c) the capacitive property is lost at high voltage and the current becomes ohmic, as in Figure 30b. This observation indicates that the system of Figure 36 contains a voltage-dependent relaxation time. Since the system is fully capacitive, the transient currents in Figure 36B do not increase, but decrease with time.

12.3. Connection of Memristors toward Networks

The combination of nanopore channels has been used to propose neural networks arrangements[22,33,155,159] and logic function circuits that perform elementary computations.[90] The utilization of nanofluidic devices for these applications is shown in **Figure 37**.[90]

The operational properties of these circuits are controlled by the hysteresis, rectification, and relaxation times that result from combining individual elements. The main properties of combined operation of rectifying channels are illustrated experimentally in **Figures 38** and **39**.[31] The memristors in series simply duplicate the original function, Figure 38a. But when connected in opposite polarities, Figure 38b, the capacitive wing of each pore dominates. The systems becomes fully capacitive, without self-crossing, and no potentiation of the conductivity occurs.[31]

The parallel combination in opposite polarity, Figure 39b, makes the high current wing dominate at each side, in consequence there is potentiation of the conductance at both positive and negative voltages, Figure 39d. At small potential the system in Figure 39b retains the capacitive property intrinsic to the chemical inductor,[68] therefore the system is doubly self-crossing.

12.4. Neurons

As commented in Section 3.2., there are different ways to make spiking elements, or neurons, for spiking networks that emulate the operation of the brain. The LIF is a capacitor that

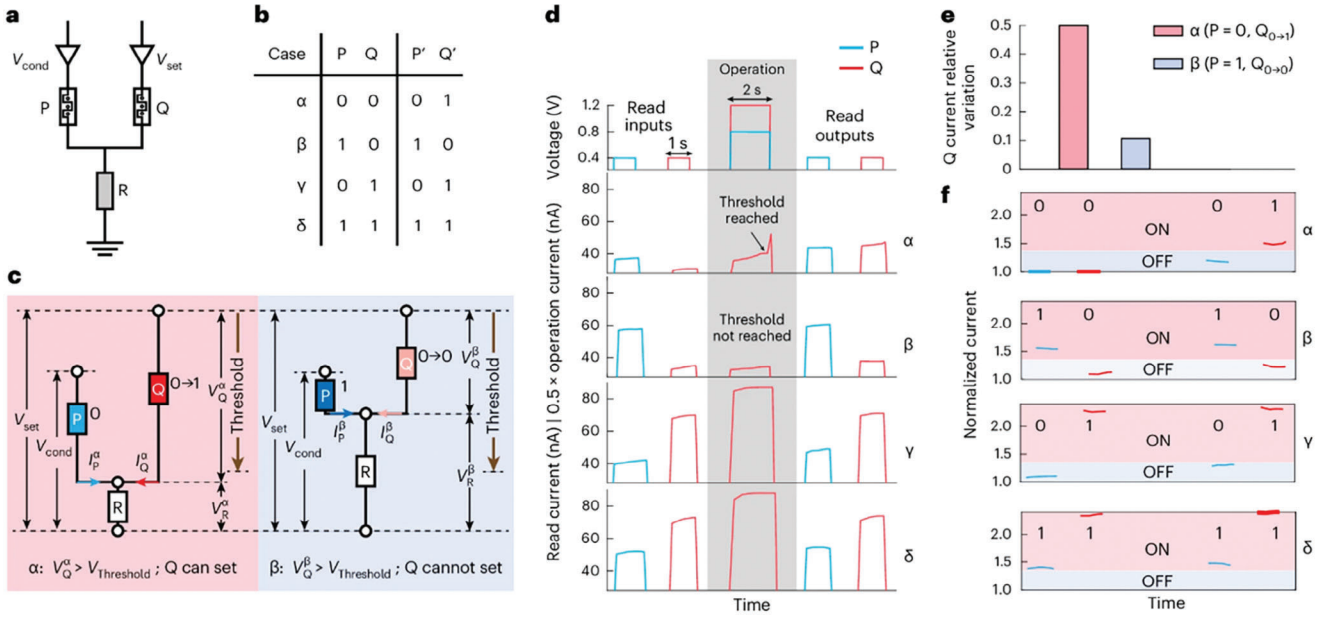

Figure 37. Nanofluidic logic. a) Circuit schematic. Two "highly asymmetric channels" HACs are connected in parallel with a variable resistor set to 6 MΩ. The working electrodes of each device are connected to the channels of a source-measurement unit. The shared ground electrode of the two cells is connected to the resistor. b) IMP truth table. The first two columns (P and Q) represent input states, and the neighboring P' and Q' columns are the corresponding outputs of the implement the material implication gate. A Greek letter is allocated to each one of the logic cases. c) Illustration of the working principle of conditional switching implementing the non-trivial cases of the IMP truth table: left, the α case and right, the β case. The effective voltage VQ applied to the Q-switch is sufficient to reach the charge threshold of the Q device within the pulse duration when P is in the 0 state (α case) and insufficient when P is in the 1 state (β case). d) Applied voltage and measured current for each logic case on both Q and P lines (Devices B and C, 1 M KCl). The measured pulses before the operation (with grey background) give the IMP table inputs and the ones after the operation provide the outputs. The Q-line current during operation reaches the threshold in the α case, indicated by an abrupt increase. e) Read current relative variations of the Q-line for the α case (rose background, P = 0) and β case, (blue background, P = 1). f) Read currents normalized by their respective minimum value in the α case both devices. The transition between the range corresponding to state 0 (blue background) and state 1 (rose background) occurs when the conductance of the corresponding device increases by at least 40% relative to its minimum value. Reproduced with permission,[90] licensed under a Creative Commons Attribution (CC BY 4.0) license.

discharges at some threshold. Bio-physical elements reproduce the sustained oscillations of the natural neurons. There is an ample variety of oscillating systems that contain a Hopf bifurcation. All of them share the combination of capacitive, inductive, and negative resistance elements.[46] A model of single oscillating ionic pore has been suggested by including activation and deactivation variables.[17] Some authors have developed oscillatory devices with electrochemical materials with properties that approach the HH neuron model, thus requiring three channels in parallel.[91,92] The combination of ionic pores has also been developed for this purpose.[15,16] In Ref. [16] the significance of the relaxation time has been well recognized. These models usually employ two rectifying channels in opposite polarities, and effective spiking is demonstrated in model calculations. We remark that the connection of inverted pores can mimic the HH neuron close to $u = 0$ in Figure 6f. However, Figure 6d,e show that both sodium and potassium channels have the large current side at positive voltage. The difference of current signs of Na and K channels is due to the suppression of the sodium current at an early stage, before it can turn upwards. The system discovered by P. Ramirez and co-workers in Figure 15,[37] using a single rectifying pore channel that is chemically deactivated, shows a close fidelity to the negative resistance feature of the neuronal sodium channel.

13. Conclusion

We developed general models describing the dominant dynamical response of rectifying nanopores, inspired by Hodgkin-Huxley neuron models and some solid state memristor models. Fluidic nanopores with an endowed charge asymmetry exhibit rectification and hysteresis. Rectification is caused by a large directional current that is observed in only one polarity, while hysteresis is caused by the relaxation of the large current branch, that can be related to the dynamics of a gating variable. These behaviors can be obtained in dynamic current-voltage and current-time curves and can be classified by the type of impedance spectra. Memristive properties are established with their connection to hysteresis phenomena, through a comprehensive analysis conducted in both the time and frequency domains. The gating variable of the pore and the associated relaxation time are the central properties determining hysteresis, transient response, synapse volatility, and neuromorphic operation in the context of multichannel devices.

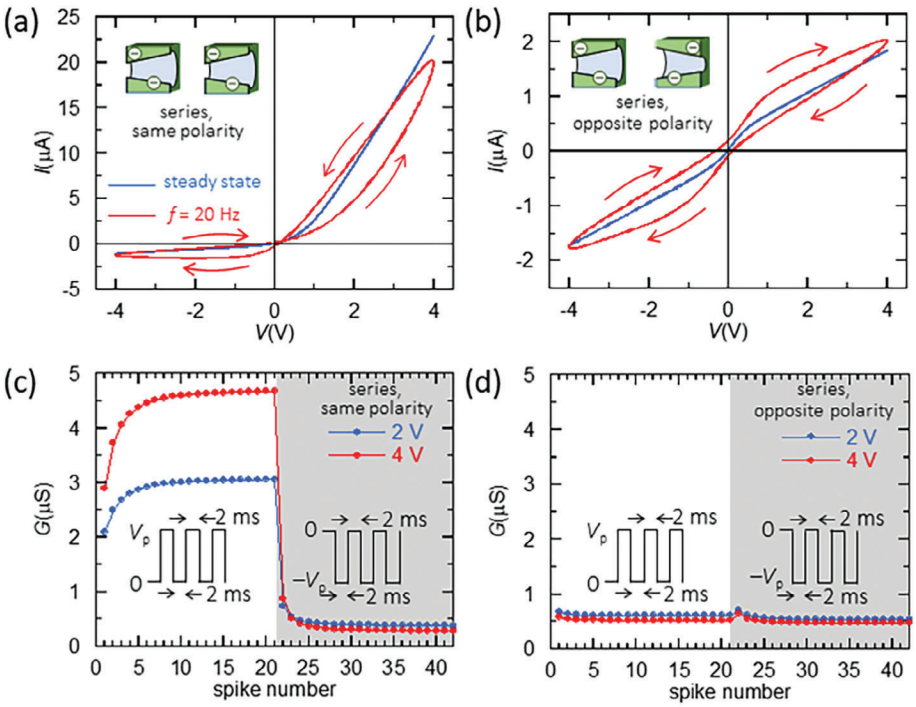

Figure 38. a) I–V curve for two polymer membrane nanopores as in Figure 9 for the series arrangement with the pores in the same polarity (inset) at $V_0 = 4$ V and $f_\Omega = 20$ Hz in a 0.1 M KCl solution (red lines). The steady-state curve (blue line) obtained at low signal frequency is also shown. b) I–V curve for the pores in the opposite polarity, facing the bases (inset). c) G versus spike number curves for the series arrangement with the pores in the same polarity. The sequences correspond to 2 ms positive and negative voltage pulses of amplitudes $V_p = 2$ V (blue curve) and 4 V (red curve). d) Conductance G versus spike number curves for the pores in the opposite polarity. Reproduced with permission.[31] Copyright 2024, American Physical Society.

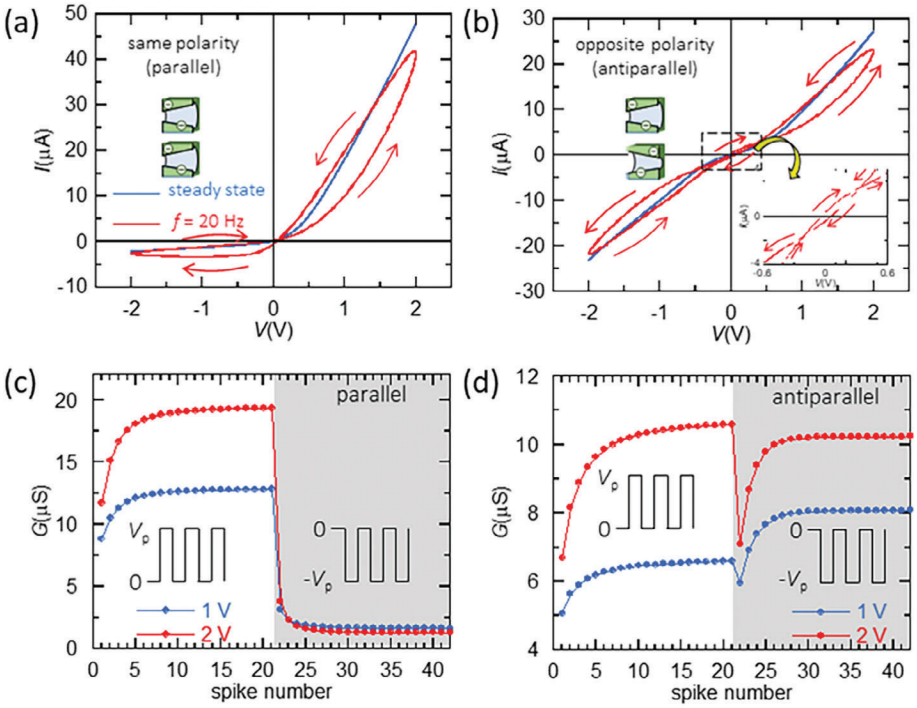

Figure 39. a) I–V curve for two polymer membrane nanopores as in Figure 9 for the parallel arrangement with the pores in the same polarity (inset) at $V_0 = 4$ V and $f_\Omega = 20$ Hz in a 0.1 M KCl solution (red lines). b) I–V curve for the parallel arrangement with the pores in opposite polarity (antiparallel). The inset zooms the central loop. c) G versus spike number curves for the parallel arrangement with the pores in the same polarity. The sequences correspond to 2 ms positive and negative voltage pulses of amplitudes $V_p = 1$ V (blue curve) and $V_p = 2$ V (red curve). d) G versus spike number curves for the antiparallel arrangement. Reproduced with permission.[31] Copyright 2024, American Physical Society.

Acknowledgements

This work was funded by the European Research Council (ERC) via Horizon Europe Advanced Grant, grant agreement n° 101097688 ("PeroSpiker").

Conflict of Interest

The author declares no conflict of interest.

Data Availability Statement

The data presented here can be accessed at https://doi.org/10.5281/zenodo.11082115 (Zenodo) under the license CC-BY-4.0 (Creative Commons Attribution-ShareAlike 4.0 International).

Keywords

hysteresis, impedance, iontronic, nanopore, neuromorphic

Received: February 22, 2024
Revised: May 16, 2024
Published online:

[1] D. V. Christensen, R. Dittmann, B. Linares-Barranco, A. Sebastian, M. Le Gallo, *Neuromorphic Comput. Eng.* **2022**, *2*, 022501.
[2] J. J. Yang, D. B. Strukov, D. R. Stewart, *Nat. Nanotechnol.* **2013**, *8*, 13.
[3] Y. Zhang, Z. Wang, J. Zhu, Y. Yang, M. Rao, W. Song, Y. Zhuo, X. Zhang, M. Cui, L. Shen, R. Huang, J. J. Yang, *Appl. Phys. Rev.* **2020**, *7*, 011308.
[4] J. Zhu, T. Zhang, Y. Yang, R. Huang, *Appl. Phys. Rev.* **2020**, *7*, 011312.
[5] M. Huang, M. Schwacke, M. Onen, J. del Alamo, J. Li, B. Yildiz, *Adv. Mater.* **2023**, *35*, 2205169.
[6] M. Lanza, A. Sebastian, W. D. Lu, M. Le Gallo, M.-F. Chang, D. Akinwande, F. M. Puglisi, H. N. Alshareef, M. Liu, J. B. Roldan, *Science* **2022**, *376*, eabj9979.
[7] J. B. Roldán, E. Miranda, D. Maldonado, A. N. Mikhaylov, N. V. Agudov, A. A. Dubkov, M. N. Koryazhkina, M. B. González, M. A. Villena, S. Poblador, M. Saludes-Tapia, R. Picos, F. Jiménez-Molinos, S. G. Stavrinides, E. Salvador, F. J. Alonso, F. Campabadal, B. Spagnolo, M. Lanza, L. O. Chua, *Adv. Intell. Syst.* **2023**, *5*, 2200338.
[8] H. Ling, D. A. Koutsouras, S. Kazemzadeh, Y. van de Burgt, F. Yan, P. Gkoupidenis, *Appl. Phys. Rev.* **2020**, *7*, 011307.
[9] Z. S. Siwy, *Adv. Func. Mater.* **2006**, *16*, 735.
[10] A. L. Hodgkin, A. F. Huxley, *J Physiol* **1952**, *117*, 500.
[11] T. F. Weiss, *Cellular Biophysics, Electrical Properties*, M.I.T. Press, Cambridge, MA **1996**.
[12] M. Häusser, *Nat. Neurosci.* **2000**, *3*, 1165.
[13] H. R. Wilson, *Spikes, Decisions, and Actions: The Dynamical Foundations of Neuroscience*, Oxford University Press, Oxford **1999**.
[14] A. J. Hopper, H. Beswick-Jones, A. M. Brown, *Adv. Physiol. Educ.* **2022**, *46*, 580.
[15] T. M. Kamsma, W. Q. Boon, T. ter Rele, C. Spitoni, R. van Roij, *Phys. Rev. Lett.* **2023**, *130*, 268401.
[16] P. Robin, N. Kavokine, L. Bocquet, *Science* **2021**, *373*, 687.
[17] J. Bisquert, *J. Phys. Chem. Lett.* **2023**, *14*, 9027.
[18] C. Li, T. Xiong, P. Yu, J. Fei, L. Mao, *ACS Appl. Bio Mater.* **2021**, *4*, 71.
[19] Y. Hou, Y. Ling, Y. Wang, M. Wang, Y. Chen, X. Li, X. Hou, *J. Phys. Chem. Lett.* **2023**, *14*, 2891.
[20] G. Pérez-Mitta, A. G. Albesa, C. Trautmann, M. E. Toimil-Molares, O. Azzaroni, *Chem. Sci.* **2017**, *8*, 890.
[21] K. Xiao, L. Wen, L. Jiang, *Small* **2016**, *12*, 2810.
[22] P. Zhang, M. Xia, F. Zhuge, Y. Zhou, Z. Wang, B. Dong, Y. Fu, K. Yang, Y. Li, Y. He, R. H. Scheicher, X. S. Miao, *Nano Lett.* **2019**, *19*, 4279.
[23] B. Sun, S. Ranjan, G. Zhou, T. Guo, C. Du, L. Wei, Y. N. Zhou, Y. A. Wu, *ACS Appl. Electron. Mater.* **2021**, *3*, 2380.
[24] S. Shchanikov, A. Zuev, I. Bordanov, S. Danilin, V. Lukoyanov, D. Korolev, A. Belov, Y. Pigareva, A. Gladkov, A. Pimashkin, A. Mikhaylov, V. Kazantsev, A. Serb, *Chaos, Solitons Fractals* **2021**, *142*, 110504.
[25] D. Shi, W. Wang, Y. Liang, L. Duan, G. Du, Y. Xie, *Nano Lett.* **2023**, *23*, 11662.
[26] M. U. Khan, G. Hassan, J. Bae, *J. Mat. Chem. C* **2020**, *8*, 13368.
[27] M. U. Khan, J. Kim, M. Y. Chougale, C. M. Furqan, Q. M. Saqib, R. A. Shaukat, N. P. Kobayashi, B. Mohammad, J. Bae, H.-S. Kwok, *Microsyst. Nanoeng.* **2022**, *8*, 56.
[28] D. Kim, J.-S. Lee, *ACS Appl. Electron. Mater.* **2023**, *5*, 664.
[29] Q. Wang, C. Zhao, Y. Sun, R. Xu, C. Li, C. Wang, W. Liu, J. Gu, Y. Shi, L. Yang, X. Tu, H. Gao, Z. Wen, *Microsyst. Nanoeng.* **2023**, *9*, 96.
[30] P. Ramirez, V. Gomez, J. Cervera, S. Mafe, J. Bisquert, *J. Phys. Chem. Lett.* **2023**, *14*, 10930.
[31] P. Ramirez, S. Portillo, J. Cervera, J. Bisquert, S. Mafe, *Phys. Rev. E* **2024**, *109*, 044803.
[32] Y. He, M. Tsutsui, Y. Zhou, X.-S. Miao, *NPG Asia Mater.* **2021**, *13*, 48.
[33] T. M. Kamsma, J. Kim, K. Kim, W. Q. Boon, C. Spitoni, J. Park, R. van Roij, *Proc. Natl. Acad. Sci. USA* **2024**, *121*, e2320242121.
[34] I. Vlassiouk, Z. S. N. D. Siwy, *Nano Lett.* **2007**, *7*, 552.
[35] D. Wang, M. Kvetny, J. Liu, W. Brown, Y. Li, G. Wang, *J. Am. Chem. Soc.* **2012**, *134*, 3651.
[36] M. R. Powell, M. Sullivan, I. Vlassiouk, D. Constantin, O. Sudre, C. C. Martens, R. S. Eisenberg, Z. S. Siwy, *Nat. Nanotechnol.* **2008**, *3*, 51.
[37] J. J. Perez-Grau, P. Ramirez, V. Garcia-Morales, J. Cervera, S. Nasir, M. Ali, W. Ensinger, S. Mafe, *ACS Appl. Mat. Int.* **2021**, *13*, 54447.
[38] G. Pérez-Mitta, W. A. Marmisollé, C. Trautmann, M. E. Toimil-Molares, O. Azzaroni, *J. Am. Chem. Soc.* **2015**, *137*, 15382.
[39] N. R. Aluru, F. Aydin, M. Z. Bazant, D. Blankschtein, A. H. Brozena, J. P. de Souza, M. Elimelech, S. Faucher, J. T. Fourkas, V. B. Koman, M. Kuehne, H. J. Kulik, H.-K. Li, Y. Li, Z. Li, A. Majumdar, J. Martis, R. P. Misra, A. Noy, T. A. Pham, H. Qu, A. Rayabharam, M. A. Reed, C. L. Ritt, E. Schwegler, Z. Siwy, M. S. Strano, Y. Wang, Y.-C. Yao, C. Zhan, Z. Zhang *Chem. Rev.* **2023**, *123*, 2737.
[40] M. Trivedi, N. Nirmalkar, *Sci. Rep.* **2022**, *12*, 2547.
[41] J. Cervera, B. Schiedt, R. Neumann, S. Mafé, P. Ramírez, *J. Chem. Phys.* **2006**, *124*, 104706.
[42] H. S. White, A. Bund, *Langmuir* **2008**, *24*, 2212.
[43] X. L. Deng, T. Takami, J. W. Son, E. J. Kang, T. Kawai, B. H. Park, *Sci. Rep.* **2014**, *4*, 4005.
[44] J. Wang, C. S. Law, S. Gunenthiran, S. Y. Lim, K. N. Vu, V. T. Ngo, K. Nielsch, A. D. Abell, A. Santos, *ACS Appl. Mat. Int.* **2023**, *15*, 45981.
[45] J. Bisquert, *PRX Energy* **2023**, *3*, 011001.
[46] J. Bisquert, *Chem. Phys. Rev.* **2023**, *4*, 031313.
[47] A. Bou, J. Bisquert, *J. Phys. Chem. B* **2021**, *125*, 9934.
[48] P. Ramirez, J. Cervera, S. Nasir, M. Ali, W. Ensinger, S. Mafe, *J. Colloid Interface Sci.* **2024**, *655*, 876.
[49] E. U. Akabuogu, L. Zhang, R. Krašovec, I. S. Roberts, T. A. Waigh, *Nano Lett.* **2024**, *24*, 2234.
[50] A. Mehonic, A. J. Kenyon, *Nature* **2022**, *604*, 255.
[51] G. Indiveri, *Neuromorphic Comput. Eng.* **2021**, *1*, 010401.
[52] W. Wang, E. Covi, A. Milozzi, M. Farronato, S. Ricci, C. Sbandati, G. Pedretti, D. Ielmini, *Adv. Intell. Syst.* **2021**, *3*, 2000224.

[53] M. Rahimi Azghadi, Y.-C. Chen, J. K. Eshraghian, J. Chen, C.-Y. Lin, A. Amirsoleimani, A. Mehonic, A. J. Kenyon, B. Fowler, J. C. Lee, Y.-F. Chang, *Adv. Intell. Syst.* **2020**, *2*, 1900189.
[54] J. Tang, F. Yuan, X. Shen, Z. Wang, M. Rao, Y. He, Y. Sun, X. Li, W. Zhang, Y. Li, B. Gao, H. Qian, G. Bi, S. Song, J. J. Yang, H. Wu, *Adv. Mater.* **2019**, *31*, 1902761.
[55] S. Jiang, S. Nie, Y. He, R. Liu, C. Chen, Q. Wan, *Mater. Today Nano* **2019**, *8*, 100059.
[56] H. Yu, H. Wei, J. Gong, H. Han, M. Ma, Y. Wang, W. Xu, *Small* **2021**, *17*, 2000041.
[57] T. V. Bliss, G. L. Collingridge, *Nature* **1993**, *361*, 31.
[58] X. Yang, Z. Xiong, Y. Chen, Y. Ren, L. Zhou, H. Li, Y. Zhou, F. Pan, S.-T. Han, *Nano Energy* **2020**, *78*, 105246.
[59] R. Kozma, R. E. Pino, G. E. Pazienza, *Advances in Neuromorphic Memristor Science and Applications*, Springer, Berlin **2012**.
[60] Y. V. Pershin, M. Di Ventra, *Adv. Phys.* **2011**, *60*, 145.
[61] M.-K. Song, J.-H. Kang, X. Zhang, W. Ji, A. Ascoli, I. Messaris, A. S. Demirkol, B. Dong, S. Aggarwal, W. Wan, S.-M. Hong, S. G. Cardwell, I. Boybat, J. Seo-s., J.-S. Lee, M. Lanza, H. Yeon, M. Onen, J. Li, B. Yildiz, J. A. del Alamo, S. Kim, S. Choi, G. Milano, C. Ricciardi, L. Alff, Y. Chai, Z. Wang, H. Bhaskaran, M. C. Hersam, D. Strukov, H. S. P. Wong, I. Valov, B. Gao, H. Wu, R. Tetzlaff, A. Sebastian, W. Lu, L. Chua, J. J. Yang, J. Kim, *ACS Nano* **2023**, *17*, 11994.
[62] R. Waser, M. Aono, *Nat. Mater.* **2007**, *6*, 833.
[63] L. Chua, *Appl. Phys. A* **2011**, *102*, 765.
[64] F. L. Aguirre, J. Suñé, E. Miranda *Micromachines*, **2022**, *13*, 330.
[65] M. Maestro-Izquierdo, M. B. Gonzalez, F. Campabadal, J. Suñé, E. Miranda, *IEEE Electron Device Lett.* **2021**, *42*, 565.
[66] E. Miranda, J. Suñé, *IEEE Trans. Nanotechnol.* **2020**, *19*, 837.
[67] L. O. Chua, K. Sung Mo, *Proc. IEEE* **1976**, *64*, 209.
[68] J. Bisquert, E. Miranda, J. B. Roldan, *Phys. Chem. Chem. Phys.* **2024**, *26*, 13804.
[69] B. Linares-Barranco, T. Serrano-Gotarredona, *Nat. Precedings* **2009**, https://doi.org/10.1038/npre.2009.3010.1031.
[70] S. H. Jo, T. Chang, I. Ebong, B. B. Bhadviya, P. Mazumder, W. Lu, *Nano Lett.* **2010**, *10*, 1297.
[71] M. Prezioso, M. R. Mahmoodi, F. M. Bayat, H. Nili, H. Kim, A. Vincent, D. B. Strukov, *Nat. Commun.* **2018**, *9*, 5311.
[72] C. Wang, Z. Si, X. Jiang, A. Malik, Y. Pan, S. Stathopoulos, A. Serb, S. Wang, T. Prodromakis, C. Papavassiliou, *IEEE J. Emerg. Selected Topics Circuits Systems* **2022**, *12*, 723.
[73] S. R. Kheradpisheh, T. Masquelier, *Int. J. Neural Syst.* **2020**, *30*, 2050027.
[74] G. Indiveri, B. Linares-Barranco, R. Legenstein, G. Deligeorgis, *Nanotechnology* **2013**, *24*, 384010.
[75] J.-Q. Yang, R. Wang, Z.-P. Wang, Q.-Y. Ma, J.-Y. Mao, Y. Ren, X. Yang, Y. Zhou, S.-T. Han, *Nano Energy* **2020**, *74*, 104828.
[76] W. Gerstner, W. M. Kistler, R. Naud, L. Paninski, *Neuronal Dynamics. From Single Neurons to Networks and Models of Cognition*, Cambridge University Press, Cambridge, MA **2014**.
[77] E. M. Izhikevich, *Dynamical Systems in Neuroscience*, MIT Press, Cambridge, MA **2007**.
[78] C. Koch, I. Segev, *Methods in Neuronal Modeling, second edition: From Ions to Networks*, MIT Press, Cambridge, MA **2003**.
[79] C. P. Fall, E. S. Marland, J. M. Wagner, J. J. Tyson (Eds.), *Computational Cell Biology*, Springer, Berlin **2002**.
[80] P. Miller, *An Introductory Course in Computational Neuroscience*, MIT Press, **2018**.
[81] W.-C. Tong, C. Y. Choi, S. Karche, A. V. Holden, H. Zhang, M. J. Taggart, *PLoS One* **2011**, *6*, e18685.
[82] S. A. Means, M. W. Roesler, A. S. Garrett, L. Cheng, A. R. Clark, *PLoS Comput. Biol.* **2023**, *19*, e1011359.
[83] W.-C. Tong, I. Ghouri, M. J. Taggart, *Front. Physiol.* **2014**, https://doi.org/10.3389/fphys.2014.00399.
[84] J. Malmivuo, R. Plonsey, *Bioelectromagnetism*, Oxford University Press, Oxford, **1995**.
[85] A. Korngreen, B. Sakmann, *J. Physiol.* **2000**, *525*, 621.
[86] D. L. Manna, A. Vicente-Sola, P. Kirkland, T. J. Bihl, G. Di Caterina, *Neuromorphic Comput. Eng.* **2022**, *2*, 044009.
[87] E. M. Izhikevich, *IEEE Trans. Neural Netw.* **2004**, *15*, 1063.
[88] X. Zhang, W. Wang, Q. Liu, X. Zhao, J. Wei, R. Cao, Z. Yao, X. Zhu, F. Zhang, H. Lv, S. Long, M. Liu, *IEEE Electron Device Lett.* **2018**, *39*, 308.
[89] R. Brette, W. Gerstner, *J. Neurophysiol.* **2005**, *94*, 3637.
[90] T. Emmerich, Y. Teng, N. Ronceray, E. Lopriore, R. Chiesa, A. Chernev, V. Artemov, M. Di Ventra, A. Kis, A. Radenovic, *Nat. Electron.* **2024**, *7*, 271.
[91] P. C. Harikesh, C.-Y. Yang, H.-Y. Wu, S. Zhang, M. J. Donahue, A. S. Caravaca, J.-D. Huang, P. S. Olofsson, M. Berggren, D. Tu, S. Fabiano, *Nat. Mater.* **2023**, *22*, 242.
[92] P. C. Harikesh, C.-Y. Yang, D. Tu, J. Y. Gerasimov, A. M. Dar, A. Armada-Moreira, M. Massetti, R. Kroon, D. Bliman, R. Olsson, E. Stavrinidou, M. Berggren, S. Fabiano, *Nat. Commun.* **2022**, *13*, 901.
[93] T. Sarkar, K. Lieberth, A. Pavlou, T. Frank, V. Mailaender, I. McCulloch, P. W. M. Blom, F. Torricelli, P. Gkoupidenis, *Nat. Electron.* **2022**, *5*, 774.
[94] J. Guckenheimer, M. Myers, *SIAM J. Sci. Comput.* **1996**, *17*, 1275.
[95] A. Mees, L. Chua, *IEEE Trans. Circuits Systems* **1979**, *26*, 235.
[96] G. Chen, J. L. Moiola, *J. Franklin Inst.* **1994**, *331*, 819.
[97] J. Wang, C. S. Law, S. Gunenthiran, H. N. Que Tran, K. N. Tran, S. Y. Lim, A. D. Abell, A. Santos, *ACS Appl. Mat. Int.* **2022**, *14*, 21181.
[98] J. Wang, K. N. Vu, A. D. Abell, A. Santos, C. S. Law, *J. Mat. Chem. C* **2023**, *11*, 9051.
[99] P. Apel, *Radiat. Meas.* **2001**, *34*, 559.
[100] Z. Siwy, A. Fuliński, *Phys. Rev. Lett.* **2002**, *89*, 198103.
[101] P. Ramirez, V. Garcia-Morales, V. Gomez, M. Ali, S. Nasir, W. Ensinger, S. Mafe, *Phys. Rev. Appl.* **2017**, *7*, 064035.
[102] W. Lee, S.-J. Park, *Chem. Rev.* **2014**, *114*, 7487.
[103] A. Santos, *J. Mat. Chem. C* **2017**, *5*, 5581.
[104] M. Norek, *J. Electrochem. Soc.* **2022**, *169*, 123503.
[105] Y. D. Kim, S. Choi, A. Kim, W. Lee, *ACS Nano* **2020**, *14*, 13727.
[106] D. Wang, W. Brown, Y. Li, M. Kvetny, J. Liu, G. Wang, *ChemElectroChem* **2018**, *5*, 3089.
[107] W. Brown, M. Kvetny, R. Yang, G. Wang, *J. Phys. Chem. C* **2022**, *126*, 10872.
[108] D. Wang, W. Brown, Y. Li, M. Kvetny, J. Liu, G. Wang, *Anal. Chem.* **2017**, *89*, 11811.
[109] J. Bisquert, *The Physics of Solar Energy Conversion*, CRC Press, Boca Raton **2020**.
[110] D. Woermann, *Nuclear Instr. Methods Phys. Res. Sec. B: Beam Inter. Mater. Atoms* **2002**, *194*, 458.
[111] C. Wen, S. Zeng, S. Li, Z. Zhang, S.-L. Zhang, *Anal. Chem.* **2019**, *91*, 14597.
[112] R. Wessel, W. B. Kristan Jr., D. Kleinfeld, *J. Neurosci.* **1999**, *19*, 5875.
[113] J. Cervera, S. Meseguer, S. Mafe, *Sci. Rep.* **2016**, *6*, 35201.
[114] J. Cervera, J. A. Manzanares, S. Mafe, *J. Phys. Chem. B* **2015**, *119*, 2968.
[115] C. C. Ceballos, A. C. Roque, R. M. Leão, *Biophys. Rev.* **2017**, *9*, 827.
[116] B. Hille, *Ion Channels of Excitable Membranes*, Sinauer Associates, Oxford **1992**.
[117] K. Williams, *Cell. Signal.* **1997**, *9*, 1.
[118] J. Bisquert, A. Bou, A. Guerrero, E. Hernández-Balaguera, *APL Machine Learning* **2023**, *1*, 036101.
[119] L. Munoz-Diaz, A. J. Rosa, A. Bou, R. S. Sanchez, B. Romero, R. A. John, M. V. Kovalenko, A. Guerrero, J. Bisquert, *Front. Energy Res.* **2022**, *10*, 914115.

[120] E. Miranda, E. Piros, F. L. Aguirre, T. Kim, P. Schreyer, J. Gehrunger, T. Oster, K. Hofmann, J. Suñé, C. Hochberger, L. Alff, *IEEE Electron Device Lett.* **2023**, *44*, 1551.
[121] C. M. Armstrong, *Q. Rev. Biophys.* **1974**, *7*, 179.
[122] A. Wacker, E. Schöll, *J. Appl. Phys.* **1995**, *78*, 7352.
[123] C. C. Ceballos, A. C. Roque, R. M. Leão, *Biophys. J.* **2017**, *113*, 2207.
[124] O. Gharbi, M. T. T. Tran, B. Tribollet, M. Turmine, V. Vivier, *Electrochim. Acta* **2020**, *343*, 136109.
[125] J. Bisquert, A. C. I. Guerrero, *J. Am. Chem. Soc.* **2022**, *144*, 5996.
[126] I. Mora-Seró, J. Bisquert, F. Fabregat-Santiago, G. Garcia-Belmonte, G. Zoppi, K. Durose, Y. Y. Proskuryakov, I. Oja, A. Belaidi, T. Dittrich, R. Tena-Zaera, A. Katty, C. Lévy-Clement, V. Barrioz, S. J. C. Irvine, *Nano Lett.* **2006**, *6*, 640.
[127] D. Klotz, *Electrochem. Comm.* **2019**, *98*, 58.
[128] Y. Bu, Z. Ahmed, L. Yobas, *Analyst* **2019**, *144*, 7168.
[129] C. Gonzales, A. Guerrero, J. Bisquert, *J. Phys. Chem. C* **2022**, *126*, 13560.
[130] J.-B. Chen, T.-T. Guo, C.-Y. Yang, J.-W. Xu, L.-Y. Gao, S.-J. Jia, P. Zhang, J.-T. Chen, Y. Zhao, J. Wang, X.-Q. Zhang, Y. Li, *J. Phys. Chem. C* **2023**, *127*, 3307.
[131] Y. Noh, A. Smolyanitsky, *J. Phys. Chem. Lett.* **2024**, *15*, 665.
[132] H. Ito, E. Schuman, *Front Neural Circuits* **2007**, https://doi.org/10.3389/neuro.04.001.2007.
[133] S. Patel, *Neuropsychopharmacology* **2012**, *37*, 583.
[134] N. Pellet, F. Giordano, M. Ibrahim Dar, G. Gregori, S. M. Zakeeruddin, J. Maier, M. Grätzel, *Prog. Photov.: Res. Appl.* **2017**, *25*, 942.
[135] J. S. Lee, S. Lee, T. W. Noh, *Appl. Phys. Rev.* **2015**, *2*, 031303.
[136] T. Chang, S.-H. Jo, W. Lu, *ACS Nano* **2011**, *5*, 7669.
[137] G. Zhou, Z. Wang, B. Sun, F. Zhou, L. Sun, H. Zhao, X. Hu, X. Peng, J. Yan, H. Wang, W. Wang, J. Li, B. Yan, D. Kuang, Y. Wang, L. Wang, *Adv. Electron. Mater.* **2022**, *8*, 2101127.
[138] S. Menzel, S. Tappertzhofen, R. Waser, I. Valov, *Phys. Chem. Chem. Phys.* **2013**, *15*, 6945.
[139] W. Chen, S. Tappertzhofen, H. J. Barnaby, M. N. Kozicki, *J. Electroceram.* **2017**, *39*, 109.
[140] F. Cüppers, S. Menzel, C. Bengel, A. Hardtdegen, M. von Witzleben, U. Böttger, R. Waser, S. Hoffmann-Eifert, *APL Mater.* **2019**, *7*, 091105.
[141] I. Fernandez-Guillen, C. A. Aranda, P. F. Betancur, M. Vallés-Pelarda, C. Momblona, T. S. Ripolles, R. Abargues, P. P. Boix, *Adv. Electron. Mater.* **2024**, *10*, 2300475.
[142] A. Franci, G. Drion, R. Sepulchre, *J. Neurophysiol.* **2017**, *119*, 1222.
[143] W. S. Russell, C.-Y. Lin, Z. S. Siwy, *ACS Appl. Nano Mater.* **2022**, *5*, 17682.
[144] M. D. Pickett, D. B. Strukov, J. L. Borghetti, J. J. Yang, G. S. Snider, D. R. Stewart, R. S. Williams, *J. Appl. Phys.* **2009**, *106*, 074508.
[145] S. Kvatinsky, E. G. Friedman, A. Kolodny, U. C. Weiser, *IEEE Trans. Circuits Systems I: Regular Papers* **2013**, *60*, 211.
[146] L. Gao, Q. Ren, J. Sun, S.-T. Han, Y. Zhou, *J. Mat. Chem. C* **2021**, *9*, 16859.
[147] A. K. Jonscher, *J. Chem. Soc. Faraday Trans. 2: Mol. Chem. Phys.* **1986**, *82*, 75.
[148] M. Ershov, H. C. Liu, L. Li, M. Buchanan, Z. R. Wasilevski, A. K. Jonsher, *IEEE Trans. Electron Devices* **1998**, *48*, 2196.
[149] E. Ehrenfreund, C. Lungenschmied, G. Dennler, H. Neugebauer, N. S. Sariciftci, *App. Phys. Lett.* **2007**, *91*, 012112.
[150] J. Bisquert, G. Garcia-Belmonte, A. Pitarch, H. Bolink, *Chem. Phys. Lett.* **2006**, *422*, 184.
[151] L. S. C. Pingree, B. J. Scott, M. T. Russell, T. J. Marks, M. C. Hersam, *App. Phys. Lett.* **2005**, *86*, 073509.
[152] F. Fabregat-Santiago, M. Kulbak, A. Zohar, M. Vallés-Pelarda, G. Hodes, D. Cahen, I. Mora-Seró, *ACS Energy Lett.* **2017**, *2*, 2007.
[153] M. T. Khan, P. Huang, A. Almohammedi, S. Kazim, S. Ahmad, *iScience* **2021**, *24*, 102024.
[154] C. Gonzales, A. Guerrero, J. Bisquert, *App. Phys. Lett.* **2021**, *118*, 073501.
[155] I. Vourkas, G. C. Sirakoulis, *IEEE Circuits Systems Mag.* **2016**, *16*, 15.
[156] P. Robin, T. Emmerich, A. Ismail, A. Niguès, Y. You, G.-H. Nam, A. Keerthi, A. Siria, A. K. Geim, B. Radha, L. Bocquet *Science* **2023**, *379*, 161.
[157] J. Bisquert, M. Sánchez-Mateu, A. Bou, C. S. Law, A. Santos, unpublished.
[158] T.-T. Guo, J.-B. Chen, C.-Y. Yang, P. Zhang, S.-J. Jia, Y. Li, J.-T. Chen, Y. Zhao, J. Wang, X.-Q. Zhang, *J. Phys. Chem. Lett.* **2024**, *15*, 2542.
[159] J. Borghetti, G. S. Snider, P. J. Kuekes, J. J. Yang, D. R. Stewart, R. S. Williams, *Nature* **2010**, *464*, 873.